

# Causal Graph Discovery

## from Self and Mutually Exciting Time Series

Song Wei<sup>a</sup>, Yao Xie<sup>a\*</sup>, Christopher S. Josef<sup>b</sup>, Rishikesan Kamaleswaran<sup>c</sup>

### Abstract

We present a generalized linear structural causal model, coupled with a novel data-adaptive linear regularization, to recover causal directed acyclic graphs (DAGs) from time series. By leveraging a recently developed stochastic monotone Variational Inequality (VI) formulation, we cast the causal discovery problem as a general convex optimization. Furthermore, we develop a non-asymptotic recovery guarantee and quantifiable uncertainty by solving a linear program to establish confidence intervals for a wide range of non-linear monotone link functions. We validate our theoretical results and show the competitive performance of our method via extensive numerical experiments. Most importantly, we demonstrate the effectiveness of our approach in recovering highly interpretable causal DAGs over Sepsis Associated Derangements (SADs) while achieving comparable prediction performance to powerful “black-box” models such as XGBoost. Thus, the future adoption of our proposed method to conduct continuous surveillance of high-risk patients by clinicians is much more likely.

**Keywords:** Causal structural learning; Directed acyclic graph; Data-adaptive approach; Generalized linear model; Granger causality.

## 1 Introduction

Continuous, automated surveillance systems incorporating machine learning models are becoming increasingly common in healthcare environments. These models can capture

---

\*Corresponding author: Yao Xie (e-mail: yao.xie@isye.gatech.edu). <sup>a</sup>Song Wei and Yao Xie are with H. Milton Stewart School of Industrial and Systems Engineering, Georgia Institute of Technology. <sup>b</sup>Christopher S. Josef is with the Department of Surgery, Emory University School of Medicine. <sup>c</sup>Rishikesan Kamaleswaran is with the Department of Biomedical Informatics, Emory University School of Medicine, and the Department of Biomedical Engineering, Georgia Institute of Technology.

temporally dependent changes across multiple patient variables and enhance a clinician’s situational awareness by providing an early warning alarm of an impending adverse event. Among those adverse events, we are particularly interested in sepsis, which is a life-threatening medical condition contributing to one in five deaths globally WHO [2020] and stands as one of the most important cases for automated in-hospital surveillance. Sepsis is formally defined as life-threatening organ dysfunction caused by a dysregulated host response to infection Singer et al. [2016]. Delays in recognizing sepsis and initiating appropriate treatment can adversely impact patient outcomes. In a recent study of adult sepsis patients, each hour of delayed treatment was associated with higher risk-adjusted in-hospital mortality (odds ratio, 1.04 per hour) Seymour et al. [2017]. Early recognition of the physiologic aberrations preceding sepsis would afford clinicians more time to intervene and may contribute to improving outcomes and reducing costs.

Recently, many machine learning methods have been developed to predict the onset of sepsis, utilizing electronic medical record (EMR) data Fleuren et al. [2020]. A recent sepsis prediction competition Reyna et al. [2019] demonstrated the robust performance of XGBoost models Du et al. [2019], Zabihi et al. [2019], Yang et al. [2020]; meanwhile, Deep Neural Networks Shashikumar et al. [2021] are also commonly used. However, most approaches offer an alert adjudicator very little information pertaining to the reasons for the prediction, leading many to refer to them as “black box” models. Thus, model predictions related to disease identification, particularly for complex diseases, still need to be adjudicated (i.e., interpreted) by a clinician before further action (i.e., treatment) can be initiated. Among the aforementioned works, Yang et al. [2020] provided one of the best attempts at identifying causality for their models’ predictions by reporting feature importance at a global level for all patients; still, this did not convey which features were most important in arriving at a given prediction for an individual patient. The common lack of interpretability of many clinical models, particularly those related to sepsis, suggests a strong need for principled methods to study the interactions among time series in medical settings.

A natural approach is to model relationships between time series and their effects on sepsis through *Granger causal graphs*. Granger causality assesses whether the history/past of one time series is predictive of another and is a popular notion of causality for time series data. Traditional approaches typically rely on a linear vector autoregressive (VAR) model Lütkepohl [2005] and consider tests on the VAR coefficients in the bivariate setting. However, it has been recognized that such traditional VAR models have many limitations, including linearity assumption Shojaie and Fox [2022] and the absence of directed acyclic graph (DAG)

structure, which is essential in causal structural learning Pearl [2009]. On the one hand, recent advancements in non-linear Granger causality consider Neural Network based approaches coupled with sparsity-inducing penalties Tank et al. [2018], Khanna and Tan [2019], but render the optimization problem non-convex. On the other hand, structural vector autoregressive (SVAR) models, which combines the structural causal model (SCM) with the VAR model, leverage DAG-inducing penalties to uncover causal DAGs. Notable contributions include Zhang and Hyvärinen [2009], Hyvärinen et al. [2010], who leveraged adaptive Lasso Zou [2006] to recover a Causal DAG, and Pamfil et al. [2020], who applied a recently proposed continuous DAG characterization Zheng et al. [2018] to encourage such DAG structure. Despite recent advancements, leveraging the well-developed convex optimization techniques to learn a causal DAG remains an open problem. Moreover, the commonly considered DAG structure is less than satisfactory since it cannot capture the lagged self-exciting components, which are important for clinicians to understand how long a node (i.e., a certain type of disease or organ dysfunction) will last once it is triggered.

In this work, we present a generalized linear structural causal model to recover the Granger causal graph from mutually exciting time series, which we call *discrete-time Hawkes network*. To encourage the desired DAG structure, we propose a novel data-adaptive linear regularizer, enabling us to cast the causal structural learning problem as a convex optimization via a monotone operator Variational Inequality (VI) formulation. Furthermore, we establish performance guarantees via recent advances in optimization Juditsky and Nemirovski [2019], Juditsky et al. [2020] by developing a non-asymptotic estimation error bound verified by numerical examples. We show the good performance of our proposed method and validate our theoretical findings using extensive numerical experiments. In particular, we demonstrate via real data experiments that our proposed method can achieve comparable prediction performance to powerful black-box methods such as XGBoost, while outputting highly interpretable Granger causal DAGs for Sepsis Associated Derangements (SADs), as shown in Figure 1. Although we only show the effectiveness of our approach in causal DAG recovery for SADs for medical applications, it can be broadly applicable to other applications.

## 1.1 Motivating application

Our work is motivated by a real study on sepsis, which contains in-hospital EMR data derived from the Grady hospital system (an academic, level 1 trauma center located in Atalanta, GA) spanning 2018-2019. The data was collected and analyzed in accordance with Emory Institutional Review Board (IRB) approved protocol #STUDY00000302. We

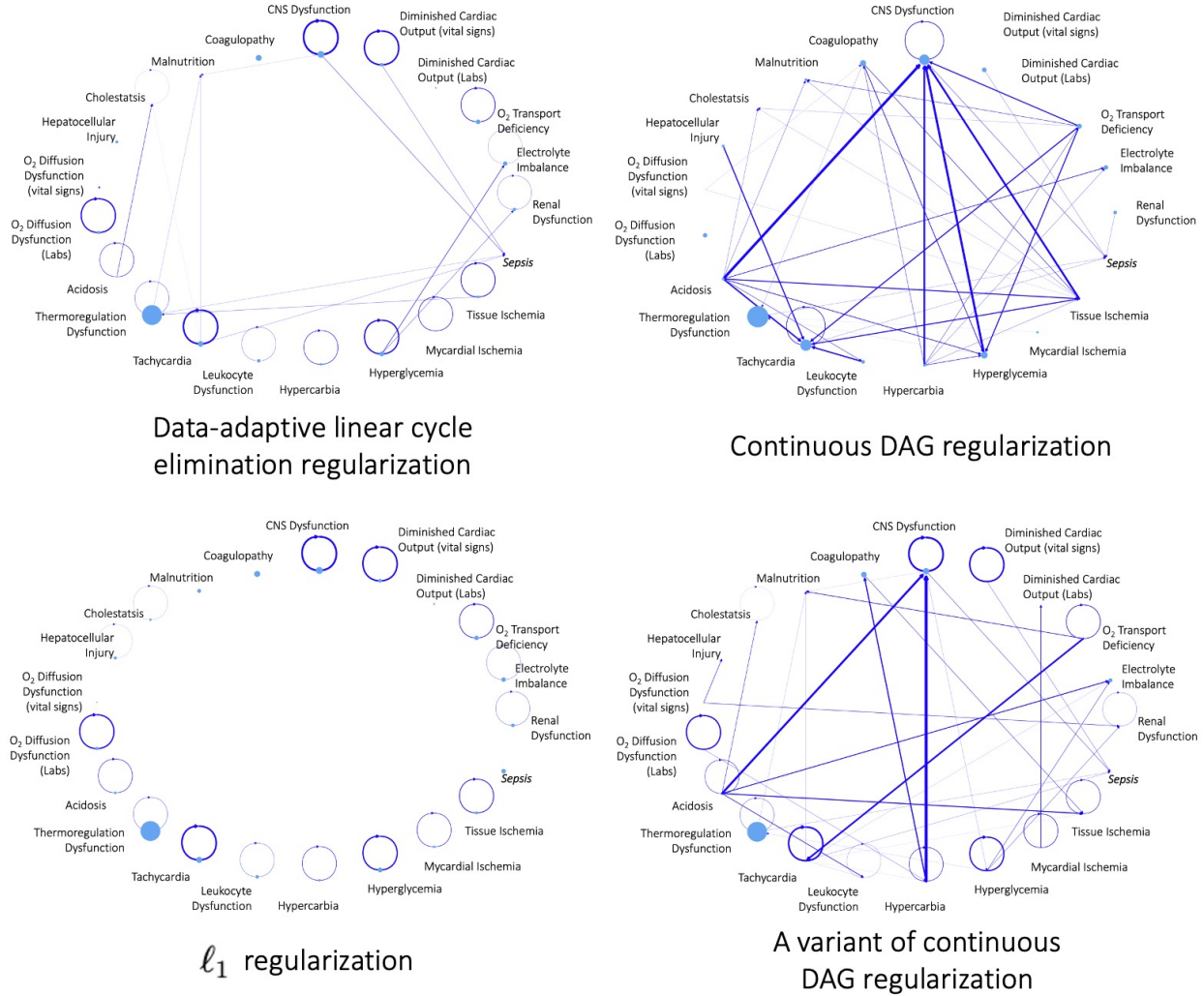


Figure 1: Causal DAGs for SADs obtained via discrete-time Hawkes network coupled with various types of regularization. The node’s size is proportional to the background intensity, and the width of the directed edge is proportional to the exciting effect magnitude. The out-of-sample AUROCs are  $0.9397$  (*proposed regularization*)  $0.9314$  (DAG regularization Zheng et al. [2018], Ng et al. [2020])  $0.9307$  (a variant of DAG regularization)  $0.9397$  ( $\ell_1$  regularization). Our proposed regularization can lead to a DAG with self-exciting edges while achieving the best prediction accuracy. However,  $\ell_1$  regularization has the same quantitative result as our proposed method; it fails to capture the interactions among SADs.

unitize a retrospective cohort of patients created in our prior work Wei et al. [2022], where the patients were included in the Sepsis-3 cohort if they met Sepsis-3 criteria while in the hospital and were admitted for more than 24 hours. The resulting descriptive statistics are provided in Table 1. The raw features of each patient include

- *Vital Signs.* In Intensive Care Unit (ICU) environments, vital signs are normally recorded at hourly intervals; however, patients on the floor may only have vital signs measured once every 8 hours.
- *Lab Results.* The laboratory tests are most commonly collected once every 24 hours; however, this collection frequency may change based on the severity of a patient’s illness.

One can find further details, such as the patient cohort construction, in Section 5 and Appendix C in Wei et al. [2022].

Table 1: Median and interquartile range (IQR) of patients demographics. Sofa score stands for Sequential Organ Failure Assessment score. The unit of time measurement for patient trajectory length is an hour.

Year	Sepsis-3 patients		Non-septic patients	
	2018 ( $n = 409$ )	2019 ( $n = 454$ )	2018 ( $n = 960$ )	2019 ( $n = 1169$ ) *
Age (median and IQR)	58 (38 - 68)	59 (46 - 68)	56 (38 - 67)	55 (37 - 66)
Gender (female percentage)	30.1%	36.6%	37.1%	35.8%
Sofa score (mean)	3.32	3.14	2.18	2.28
Trajectory length (median and IQR)	25 (25 - 25)	25 (25 - 25)	17 (13 - 22)	17 (13 - 22)

\*  $n$  represents the total number of patients in the corresponding cohort.

Our goal is to construct a predictive model for sepsis and an interpretable causal DAG estimation that captures the interactions among those vital signs and Lab results. One difficulty comes from synchronous and continuous-valued observations assumption — in many real applications, especially in the medical setting, the observations can be both continuous and categorical-valued. They can also be asynchronous and sampled with different frequencies. For example, vital signs are recorded regularly, whereas Lab results are only ordered when clinically necessary. Since the absence of a lab carries meaning itself, this cannot be simply formulated into a missing data problem.

One approach to obtaining interpretable predictive models is to consider their syndromic nature — there is often a constellation of different physiologic derangements that can combine

to create the condition. For example, our prior works Wei et al. [2021a, 2022] leveraged expert opinion to identify the distinct types of measurable, physiologic change that accompanies sepsis-related illness, which is called Sepsis Associated Derangements; see the definitions of SADs in Table 4. However, the clinician did not determine the relationship among the SADs; rather, these relationships were an output of model fitting. Although there is a recently proposed principled method to handle such mixed-frequency time series Tank et al. [2019], we adopt a similar approach with Wei et al. [2022] in this study based on expert advice.

## 1.2 Literature

In this subsection, we briefly review several closely related areas and defer an extended literature survey to Appendix A.

*Causal structural learning.* Structural causal model-based causal discovery methods often boil down to maximizing a score function within the DAG family Glymour et al. [2019], making efficient DAG learning fundamental to causal discovery. However, learning DAGs from observational data, i.e., the structural learning problem, is NP-hard due to the combinatorial acyclicity constraint Chickering et al. [2004]. This motivated many research efforts to find efficient approaches for learning DAGs. Recently, Yuan et al. [2019] proposed an indicator function-based approach to enumerate and eliminate all possible directed cycles; they used truncate  $\ell_1$ -function as a continuous surrogate of indicator function and proposed to use alternating direction method of multipliers to solve the problem numerically. Later on, Manzour et al. [2021] followed this approach, transferred indicators into binary variables, and leveraged mixed integer programming to solve the problem. In addition, there are also dynamic programming-based approaches, e.g., Loh and Bühlmann [2014], but they are not scalable in high dimensions unless coupled with a sparsity-inducing penalty, e.g.,  $A^*$  Lasso Xiang and Kim [2013].

One notable recent contribution in structural learning is Zheng et al. [2018], who formulated the DAG recovery problem as a constrained continuous optimization via a smooth DAG characterization; they applied an augmented Lagrangian method to transfer constraint as penalty and achieved efficient DAG recovery. Later on, Ng et al. [2020] proposed to use the non-convex DAG characterization as a penalty directly and showed an asymptotic recovery guarantee for linear Gaussian models. Other notable extensions along this direction include a discrete backpropagation method, exploration of low-rank structure Fang et al. [2020] and neural DAG learning Yu et al. [2019], Ke et al. [2019], Lachapelle et al. [2019]. We refer

readers to Scanagatta et al. [2019], Schölkopf et al. [2021], Kitson et al. [2021], Vowels et al. [2022] for systematic surveys on structural learning and causal discovery.

We would like to highlight that our approach considers DAG structure with lagged self-exciting components in this work is new in the literature. Existing works typically allow directed cycles in the adjacency matrices representing the lagged effects Zhang and Hyvärinen [2009], Hyvärinen et al. [2010], Pamfil et al. [2020], Tong et al., Wei et al. [2022]. As a question of science, we believe those lagged cycles are less explainable. For example, our prior work Wei et al. [2022] discovered a “Renal Dysfunction  $\rightarrow$  O<sub>2</sub> Diffusion Dysfunction  $\rightarrow$  Renal Dysfunction” cyclic chain pattern, but we believe the “Renal Dysfunction  $\rightarrow$  O<sub>2</sub> Diffusion Dysfunction” coupled with the self-exciting pattern of Renal Dysfunction uncovered by our proposed method here is more convincing; see the bottom right panel in Figure 1.

*Granger causality for time series.* One line of research Lütkepohl [2005] combines SCM and VAR models and develops the so-called structural vector autoregressive models to help uncover the Granger causal graphs with certain desired structures, such as DAG structure. Notable contributions include Zhang and Hyvärinen [2009], Hyvärinen et al. [2010], who applied adaptive Lasso Zou [2006] to encourage the DAG structure. Moreover, following Shimizu et al. [2006], Hyvärinen et al. [2010] extended the finding that the non-Gaussian measurement noise helps the model identifiability to time series setting; later on, Tank et al. [2019] further proved identifiability of SVAR models of order one under arbitrary subsampling and mixed frequency scheme. In addition to adaptive Lasso, there are also other approaches to encouraging DAG structure in the SVAR model, such as the aforementioned continuous DAG characterization Pamfil et al. [2020]. As a comparison, our proposed generalized liner model (GLM) can be reformulated into a *stochastic* SCM by using Gumbel-Max trick/technique Maddison et al. [2017], Jang et al. [2017], Oberst and Sontag [2019], Lorberbom et al. [2021], Noorbakhsh and Rodriguez [2021], which is slightly different from the *deterministic* SCMs with measurement noise in SVAR models Zhang and Hyvärinen [2009], Hyvärinen et al. [2010], Pamfil et al. [2020]. Moreover, compared with the commonly adopted DAG-inducing penalties in SVAR models, e.g., the continuous, differentiable but non-convex DAG characterization Zheng et al. [2018], our proposed data-adaptive linear method for structural learning approach is not only convex but also flexible in the sense that it can encourage a DAG structure while keeping lagged self-exciting components.

Another line of research focuses on nonlinear Granger causality. Common nonlinear approaches consider additive nonlinear effects from history that decouple across multiple time series, such as Sindhvani et al. [2013], which leveraged a separable matrix-valued kernel to

infer the nonlinear Granger causality. To further capture the potential nonlinear interactions between predictors, Neural Networks coupled with sparsity-inducing penalties are adopted Tank et al. [2018], Khanna and Tan [2019]. Even though our GLM can be viewed as a Neural Network without a hidden layer, our model is convex, theoretically grounded, and easy to train, which are the major advantages over Neural Network-based methods. In addition, there are also efforts to tackle the high-dimensionality via regularization, such as group Lasso Bolstad et al. [2011], Basu et al. [2015] and nuclear norm regularization Basu et al. [2019]. For a comprehensive survey on Granger causality, we refer readers to Shojaie and Fox [2022].

### 1.3 Notations

Our notations are conventional. We use  $\mathbb{R}_+$  to denote the collection of non-negative real numbers, i.e.,  $\mathbb{R}_+ = [0, \infty)$ . For integers  $0 < m \leq n$ , we denote  $[m : n] = \{m, \dots, n\}$ ; in a special case where  $m = 1$ , we denote  $[n] = \{1, \dots, n\}$ . Superscript  $\top$  denotes vector/matrix transpose; column vectors  $\mathbf{1}_d = (1, \dots, 1)^\top \in \mathbb{R}^d$ ,  $\mathbf{0}_d = (0, \dots, 0)^\top \in \mathbb{R}^d$ ,  $e_{i,d} \in \mathbb{R}^d$  is the standard basis vector with its  $i$ -th element being one and matrix  $I_d \in \mathbb{R}^{d \times d}$  denotes the  $d$ -by- $d$  identity matrix;  $\text{tr}(e^A)$  stands for the trace of the matrix exponential of matrix  $A$ . For vectors  $a, b \in \mathbb{R}^d$ , the comparison  $a \leq b$  is element-wise. In addition, we use  $\nabla$  to denote the derivative operator; we use  $\langle \cdot, \cdot \rangle$  to denote the standard inner product in Euclidean space,  $\|\cdot\|_p$  to denote the vector  $\ell_p$  norm and  $\|\cdot\|_F$  to denote the matrix  $F$ -norm.

## 2 Discrete-Time Hawkes Network

### 2.1 Set-up and Background

Consider mixed-type observations over a time horizon  $T \geq 1$ : we observe (i)  $d_1$  sequences of binary time series  $\{y_1^{(i)}, \dots, y_T^{(i)}\}$ ,  $i \in [d_1]$ , which represent  $d_1$  type of events' occurrences, (ii)  $d_2$  sequences of continuous-values time series  $\{x_1^{(i)}, \dots, x_T^{(i)}\}$ ,  $i \in [d_2]$ , and (iii)  $d_3$  static variables  $z_1, \dots, z_{d_3}$ . In the following, we will refer to the binary variable as node variables, and our primary goal is to recover the graph structure over those  $d_1$  nodes.

*Linear multivariate Hawkes process (MHP) model for time series.* The MHP models the mutual inter-dependence among variables by considering a conditional intensity of event occurrence, which is jointly determined by a deterministic background and a self-exciting (or inhibiting) term depending on its history observations. Given that the intensity has a natural interpretation as the instantaneous probability and is inspired by linear MHP with



the exponential decaying kernel, we model the probability of occurrence for the  $i$ -th node variable,  $i \in [d_1]$ , at time step  $t \in [2 : T]$  as follows:

$$\mathbb{P}(y_t^{(i)} = 1 | \mathcal{H}_{t-1}) = \nu_i + \sum_{j=1}^{d_3} \gamma_{ij} z_j + \sum_{k=1}^{t-1} \left( \sum_{j=1}^{d_2} \beta_{ij} x_{t-k}^{(j)} e^{-Rk} + \sum_{j=1}^{d_1} \alpha_{ij} y_{t-k}^{(j)} e^{-Rk} \right), \quad (1)$$

where  $\mathcal{H}_t$  denotes the history observation up to time  $t$ . To ensure the right-hand side (RHS) of the above equation is a valid probability, we add the following constraint:

$$0 \leq \nu_i + \sum_{j=1}^{d_3} \gamma_{ij} z_j + \sum_{k=1}^{t-1} \left( \sum_{j=1}^{d_2} \beta_{ij} x_{t-k}^{(j)} e^{-Rk} + \sum_{j=1}^{d_1} \alpha_{ij} y_{t-k}^{(j)} e^{-Rk} \right) \leq 1. \quad (2)$$

*Interpretation of parameters.* For the  $i$ -th node variable,  $\gamma_{ij} \in \mathbb{R}$  represents the influence from  $j$ -th static variable and contributes to the deterministic background intensity together with  $\nu_i \in \mathbb{R}_+$ ; parameter  $\alpha_{ij} \in \mathbb{R}$  (or  $\beta_{ij} \in \mathbb{R}$ ) represents the magnitude of the influence from the  $j$ -th node variable (or continuous variable) to the  $i$ -th node variable, which decays exponentially fast with exponent characterized by  $R > 0$  — those parameter interpretations connect (1) with the conditional intensity function of the MHP, e.g., Wei et al. [2022]. Moreover, one advantage of the above model is that, as long as (2) is satisfied, we do not restrict  $\alpha_{ij}$  or  $\beta_{ij}$  to be non-negative, meaning that our model can handle both triggering and inhibiting effects.

*Graph terminology.* The matrix  $A = (\alpha_{ij}) \in \mathbb{R}^{d_1 \times d_1}$  defines a weighted directed graph  $\mathcal{G}(A) = (\mathcal{V}, \mathcal{E})$  on  $d_1$  nodes in the following way:  $\mathcal{V}$  is the collection of aforementioned  $d_1$  binary node variables; let  $\mathcal{A} \in \{0, 1\}^{d_1 \times d_1}$  such that  $\mathcal{A}_{ij} = 1$  if  $\alpha_{ij} \neq 0$  and zero otherwise, then  $\mathcal{A}$  defines the adjacency matrix of a directed graph  $\mathcal{G}(A)$ , which gives the collection of directed edges  $\mathcal{E}$ ; the weights of the directed edges in  $\mathcal{E}$  are defined accordingly by matrix  $A$ . In a slight abuse of notation, we will treat  $A$  as if it were a (weighted) graph or the (weighted) adjacency matrix of the graph.

## 2.2 Linear model

One drawback of MHP comes from its scalability; to be precise, considering complete history leads to quadratic complexity with respect to (w.r.t.) the number of events. Since the triggering (or inhibiting) effects from the history observations decay exponentially fast, we typically consider finite memory depth. Similarly, in our discrete-time Hawkes network, we make reasonable simplification by assuming *finite memory depth*  $\tau \geq 1$  for both continuous

and binary observations. More specifically, consider given history at time  $t \in [1 - \tau : 0]$ . At time  $t \in [T]$ , we use  $w_{t-\tau:t-1}$  to denote the observations from  $t - \tau$  to  $t - 1$ :

$$w_{t-\tau:t-1} = \left(1, z_1, \dots, z_{d_3}, x_{t-1}^{(1)}, \dots, x_{t-\tau}^{(1)}, \dots, x_{t-1}^{(d_2)}, \dots, x_{t-\tau}^{(d_2)}, y_{t-1}^{(1)}, \dots, y_{t-\tau}^{(1)}, \dots, y_{t-1}^{(d_1)}, \dots, y_{t-\tau}^{(d_1)}\right)^\top.$$

For brevity, we denote  $\alpha_{ijk} = \alpha_{ij} \exp\{-Rk\}$  and  $\beta_{ijk} = \beta_{ij} \exp\{-Rk\}$ . Then, we can rewrite (1) into the following compact form:

$$\begin{aligned} \mathbb{P}\left(y_t^{(i)} = 1 \mid w_{t-\tau:t-1}\right) &= w_{t-\tau:t-1}^\top \theta_i, \\ \theta_i \in \Theta &= \{\theta : 0 \leq w_{t-\tau:t-1}^\top \theta \leq 1, t \in [T]\} \subset \mathbb{R}^d, \end{aligned} \quad (3)$$

where  $d = 1 + d_3 + \tau d_2 + \tau d_1$  is the dimensionality,  $\Theta$  is the feasible region, and  $\theta_i$  is the model parameter:

$$\theta_i = (\nu_i, \gamma_{i1}, \dots, \gamma_{id_3}, \beta_{i11}, \dots, \beta_{i1\tau}, \dots, \beta_{id_21}, \dots, \beta_{id_2\tau}, \alpha_{i11}, \dots, \alpha_{i1\tau}, \dots, \alpha_{id_11}, \dots, \alpha_{id_1\tau})^\top.$$

This parameter summarizes the influence from all variables to the  $i$ -th node. Before we move on, we want to briefly mention that, as a special case of the generalized linear model, (3) can also be re-parameterized into a causal structural model and its parameters  $A_k = (\alpha_{ijk}) \in \mathbb{R}^{d_1 \times d_1}$ ,  $k \in [\tau]$ , can be taken as Granger causal graphs under the no unobserved confounder assumption. We will elaborate on these in Section 2.3. Now, let us present the estimation method using VI.

*Estimation.* We leverage a recently developed technique Juditsky and Nemirovski [2019], Juditsky et al. [2020], which estimates the model parameters by solving stochastic monotone Variational Inequality, to develop a statistically principled estimator for discrete-time Hawkes network. To be precise, in our linear model (3), for  $i \in [d_1]$ , we use the weak solution to the following VI as the estimator  $\hat{\theta}_i$ :

$$\text{find } \hat{\theta}_i \in \Theta : \langle \bar{F}_T^{(i)}(\theta_i), \theta_i - \hat{\theta}_i \rangle \geq 0, \quad \forall \theta_i \in \Theta, \quad \text{VI}[\bar{F}_T^{(i)}, \Theta]$$

where  $\bar{F}_T^{(i)}(\theta_i)$  is the empirical vector field defined as follows:

$$\bar{F}_T^{(i)}(\theta_i) = \frac{1}{T} \sum_{t=1}^T w_{t-\tau:t-1} w_{t-\tau:t-1}^\top \theta_i - \frac{1}{T} \sum_{t=1}^T w_{t-\tau:t-1} y_t^{(i)} = \mathbb{W}_{1:T} \theta_i - \frac{1}{T} \sum_{t=1}^T w_{t-\tau:t-1} y_t^{(i)}, \quad (4)$$

and

$$\mathbb{W}_{1:T} = \frac{1}{T} \sum_{t=1}^T w_{t-\tau:t-1} w_{t-\tau:t-1}^\top \in \mathbb{R}^{d \times d}. \quad (5)$$

*Connection to LS estimator.* One important observation is that the vector field  $\bar{F}_T^{(i)}(\theta_i)$  (4) is indeed the gradient field of the Least Square objective, meaning that the weak solution to the corresponding VI solves the following LS problem Juditsky et al. [2020]:

$$\begin{aligned} \min_{\theta_i} \quad & \frac{1}{2T} \|\mathbf{w}_{1:T}^\top \theta_i - Y_{1:T}^{(i)}\|_2^2, \\ \text{subject to} \quad & \mathbf{0}_T \leq \mathbf{w}_{1:T}^\top \theta_i \leq \mathbf{1}_T, \end{aligned} \quad (6)$$

where

$$\mathbf{w}_{1:T} = (w_{1-\tau:0}, \dots, w_{T-\tau:T-1}) \in \mathbb{R}^{d \times T}, \quad Y_{1:T}^{(i)} = (y_1^{(i)}, \dots, y_T^{(i)})^\top \in \mathbb{R}^T. \quad (7)$$

*Solving for LS estimator.* One approach to solve (6) is to leverage the well-developed convex optimization tools, such as CVX Grant and Boyd [2014] and Mosek ApS [2019]. An alternative approach is through projected gradient descent (PGD), where the empirical vector field (4) is treated as the gradient field. To be precise, we introduce dual variables  $\eta_1 = (\eta_{1,1}, \dots, \eta_{1,T})^\top \in \mathbb{R}_+^T$ ,  $\eta_2 = (\eta_{2,1}, \dots, \eta_{2,T})^\top \in \mathbb{R}_+^T$  and the Lagrangian is given by:

$$L(\theta_i, \eta_1, \eta_2) = \frac{1}{2T} \|\mathbf{w}_{1:T}^\top \theta_i - Y_{1:T}^{(i)}\|_2^2 + \eta_1^\top (\mathbf{w}_{1:T}^\top \theta_i - \mathbf{1}_T) - \eta_2^\top \mathbf{w}_{1:T}^\top \theta_i.$$

The Lagrangian dual function is  $\min_{\theta_i} L(\theta_i, \eta_1, \eta_2)$ . As we can see, the Lagrangian above is convex w.r.t.  $\theta_i$ . By setting  $\nabla_{\theta_i} L(\theta_i, \eta_1, \eta_2) = 0$ , we have

$$\hat{\theta}_i(\eta_1, \eta_2) = \frac{1}{T} \mathbb{W}_{1:T}^{-1} \left( \mathbf{w}_{1:T} Y_{1:T}^{(i)} / T - \eta_1 + \eta_2 \right).$$

As pointed out in Juditsky et al. [2020],  $\mathbb{W}_{1:T} \in \mathbb{R}^{d \times d}$  (5) will be full rank (and thus invertible) with high probability when  $T$  is sufficiently large. By plugging  $\hat{\theta}_i(\eta_1, \eta_2)$  into the Lagrangian, we give the dual problem as follows:

$$\begin{aligned} \max_{\eta_1, \eta_2} \quad & L(\hat{\theta}_i(\eta_1, \eta_2), \eta_1, \eta_2), \\ \text{subject to} \quad & \eta_1, \eta_2 \geq \mathbf{0}_T. \end{aligned}$$

This problem can be solved by PGD as its projection step simply changes all negative entries to zeros.

## 2.3 Generalized linear model

As mentioned earlier, the linear assumption is restrictive, and therefore, we consider the following generalized linear model Efron [2022] to enhance its expressiveness:

$$\mathbb{P}\left(y_t^{(i)} = 1 \mid w_{t-\tau:t-1}\right) = g\left(w_{t-\tau:t-1}^\top \theta_i\right), \quad \theta_i \in \Theta, \quad (8)$$

where  $g : \mathbb{R} \rightarrow [0, 1]$  is a monotone *link function*. For example, it can be non-linear, such as sigmoid link function  $g(x) = 1/(1 + e^{-x})$  on a domain  $x \in \mathbb{R}$  and exponential link function  $g(x) = 1 - e^{-x}$  on a domain  $x \in \mathbb{R}_+$ ; also, it can be linear  $g(x) = x$  on a domain  $x \in [0, 1]$ , which reduces our GLM (8) to the linear model (3). The feasible region  $\Theta$  will vary based on the choice of link functions, and we will see two examples later in Section 2.4.

**Remark 1** (Re-parameterization as a structural causal model). Gumbel-Max SCM, which re-parameterizes the probability function of a Bernoulli random variable (r.v.) into an SCM via the Gumbel-Max technique Maddison et al. [2017], Jang et al. [2017], can help uncover the connection between the GLM (8) and the stochastic SCM. Let us denote

$$p_t^{(i)}(1) = \mathbb{P}\left(y_t^{(i)} = 1 \mid w_{t-\tau:t-1}\right) = g\left(w_{t-\tau:t-1}^\top \theta_i\right), \quad p_t^{(i)}(0) = 1 - p_t^{(i)}(1).$$

Then, our GLM (8) can be reformulated into an SCM as follows:

$$y_t^{(i)} = \arg \max_{y \in \{0,1\}} \left( \log(p_t^{(i)}(y)) + \epsilon_t^{(i)} \right), \quad (9)$$

where  $\epsilon_t^{(i)}$  is a Gumbel r.v., i.e.,  $\epsilon_t^{(i)} \sim \text{Gumbel}(0, 1)$ . The Gumbel-Max technique tells us that that the SCM (9) is equivalent to our GLM (8) in that we still have  $\mathbb{P}(y_t^{(i)} = 1 \mid w_{t-\tau:t-1}) = g\left(w_{t-\tau:t-1}^\top \theta_i\right)$ .

*Non-linear Granger causality.* By the definition of Granger causality in non-linear autoregressive model Tank et al. [2018], adjacency matrices  $A_k = (\alpha_{ijk}) \in \mathbb{R}^{d_1 \times d_1}$ ,  $k \in [\tau]$ , represent the Granger causal graph structure over  $d_1$  nodes. To be precise, the Granger non-causality can be obtained as follows:

**Proposition 1.** Time series  $\{y_t^{(j)}, t \in [T]\}$  is Granger non-causal for time series  $\{y_t^{(i)}, t \in [T]\}$  if and only if (iff)  $\alpha_{ijk} = 0$  for all  $k \in [\tau]$  in our generalized linear model (8).

We need to mention that inferring Granger causality needs “all the information in the universe” and hence we can only infer Granger non-causality and *prima facie causality* given

partially observed data Granger [1969, 1980, 1988]. In the graph induced by  $A_k = (\alpha_{ijk}), k \in [\tau]$ , the absence of an edge means Granger non-causality, whereas the presence of an edge in  $A$  only implies prima facie causality. In this work, we will assume there is *no unobserved confounding* and we say time series  $\{y_t^{(j)}, t \in [T]\}$  Granger causes time series  $\{y_t^{(i)}, t \in [T]\}$  if there exists  $k \in [\tau]$  such that  $\alpha_{ijk} \neq 0$ .

## 2.4 Estimation with Variational Inequality

Similar to  $\text{VI}[\bar{F}_T^{(i)}, \Theta]$  for the linear model, we use the weak solution to the following VI as the estimator for our GLM (8):

$$\text{find } \hat{\theta}_i \in \Theta : \langle F_T^{(i)}(\theta_i), \theta_i - \hat{\theta}_i \rangle \geq 0, \forall \theta_i \in \Theta, \quad \text{VI}[F_T^{(i)}, \Theta]$$

Parameter  $\theta_i$  is constrained in a convex set  $\Theta \subset \mathbb{R}^d$ , which may vary with different non-linear links; we will see two examples later. The main difference from  $\text{VI}[\bar{F}_T^{(i)}, \Theta]$  is the empirical vector field, which is defined as follows:

$$F_T^{(i)}(\theta_i) = \frac{1}{T} \sum_{t=1}^T w_{t-\tau:t-1} \left( g(w_{t-\tau:t-1}^\top \theta_i) - y_t^{(i)} \right). \quad (10)$$

As we can see, the definition above covers that of  $\bar{F}_T^{(i)}$  (4) for linear link case; thus, we will use  $F_T^{(i)}$  to denote the empirical vector field for all monotone links in the following. Furthermore, the statistical inference for each node can be *decoupled*, and thus we can perform parallel estimation and simplify the analysis.

The intuition behind this VI-based method is straightforward. Let us consider the global counterpart of the above vector field, whose root is the unknown ground truth  $\theta_i^*$ , i.e.,

$$F^{(i)}(\theta_i) = \mathbb{E}_{(w,y^{(i)})} [w (g(w^\top \theta_i) - y^{(i)})] = \mathbb{E}_{(w,y^{(i)})} [w (g(w^\top \theta_i) - g(w^\top \theta_i^*))].$$

Although we cannot access this global counterpart, by solving the empirical one  $\text{VI}[F_T^{(i)}, \Theta]$  we could approximate the ground truth very well. We will show how well this approximation can be in Section 4.

**Remark 2** (Comparison with the original work). As a generalization of the VI-based estimator for binary time series Juditsky et al. [2020], our method can handle mix-type data (i.e., binary and continuous-valued time series and static variables). Furthermore, we show how to leverage regularization in the VI-based estimation framework as well as extend

the performance guarantee to general non-linear monotone link functions, on which we will elaborate in Sections 3 and 4, respectively.

*Examples for non-linear link function.* Now, we will give two examples of general non-linear monotone links and briefly discuss how to numerically obtain our proposed estimator. Note that the equivalence between our proposed estimator and LS estimator only holds for linear link function since the gradient field of LS objective with general link function will be:

$$\frac{1}{T} \sum_{t=1}^T \nabla g(w_{t-\tau:t-1}^T \theta_i) \left( g(w_{t-\tau:t-1}^T \theta_i) - y_t^{(i)} \right) = \frac{1}{T} \sum_{t=1}^T w_{t-\tau:t-1} g'(w_{t-\tau:t-1}^T \theta_i) \left( g(w_{t-\tau:t-1}^T \theta_i) - y_t^{(i)} \right),$$

where  $g'$  is the derivative of  $g$ . However, in the sigmoid link function special case, our proposed estimator reduces to the Maximum Likelihood estimator for the logistic regression. To be precise, we can show that the empirical vector field (10) is the gradient field of the objective function of the following ML problem:

$$\max_{\theta_i} \frac{1}{T} \sum_{t=1}^T y_t^{(i)} \log g(w_{t-\tau:t-1}^T \theta_i) + (1 - y_t^{(i)}) \log (1 - g(w_{t-\tau:t-1}^T \theta_i)).$$

Again, this equivalence between our proposed estimator and ML estimator comes from the fact that  $g'(x) = g(x)(1 - g(x))$  for the sigmoid link function and does not hold for other non-linear link functions.

One advantage of the sigmoid link function is that we do not need to put additional constraints on the parameter  $\theta_i$  to ensure  $g(w_{t-\tau:t-1}^T \theta_i)$  is a reasonable probability, i.e., the feasible region is  $\Theta = \mathbb{R}^d$ . To numerically obtain such our proposed estimator, we can use vanilla gradient descent, where the gradient is the empirical vector field (10).

Another non-linear link example is the exponential link  $g(x) = 1 - e^{-x}$ ,  $x \in \mathbb{R}_+$ . Similar to the linear link case, to ensure valid probability, the feasible region is  $\Theta = \{\theta : w_{t-\tau:t-1}^T \theta \geq 0, t \in [T]\}$ . To numerically solve for our proposed estimator, we can again perform PGD on the Lagrangian dual problem. Alternatively, in many real applications where we have prior knowledge that we do not consider inhibiting effect, i.e., the feasible region is  $\theta_i \in \mathbb{R}_+^d \subset \Theta$ , we can perform PGD on the primal problem.

For general non-linear links, PGD is the most sensible approach to obtain our proposed estimator. However, due to the serial correlation in the data, we cannot conduct theoretical convergence analysis as Juditsky and Nemirovski [2019] did. Later in Section 5.2, we will use numerical simulation to demonstrate the good performance of PGD for all three

aforementioned link functions.

### 3 Data-Adaptive Linear Structural Learning

In causal structural learning Pearl [2009], it is often of great interest to recover a directed acyclic graph from observational data. In our analysis, slightly different from a DAG, we want a DAG-like structure that additionally keeps the lagged self-exciting components, i.e., length-1 cycles. This is because a stronger self-exciting effect informs the adjudicator that the corresponding node/event can last for a longer time once triggered. Therefore, our goal is to remove the less explainable directed cycles with lengths greater than or equal to two while keeping lagged self-exciting components to improve the result interpretability. In the following, we call directed cycles with lengths greater or equal to two as cycles for brevity.

#### 3.1 Data-adaptive linear cycle elimination regularization

Consider the Granger causal graphs induced by the estimated adjacency matrices  $\hat{A}_\ell = (\hat{\alpha}_{ij\ell}) \in \mathbb{R}^{d_1 \times d_1}$ ,  $\ell \in [\tau]$ , using the VI-based estimator  $\text{VI}[F_T^{(i)}, \Theta]$ . As mentioned earlier, cycles in those graphs are undesirable, and we want to remove them. Let us begin with formally defining cycles: for positive integer  $L \geq 2$ , if there exist  $\ell \in [\tau]$  and mutually different indices  $i_1, \dots, i_L \in [d_1]$  such that

$$\hat{\alpha}_{i_1 i_L \ell} > 0, \quad \hat{\alpha}_{i_{k+1} i_k \ell} > 0, \quad k \in [L - 1],$$

then we say there exists a length- $L$  (directed) cycle in the directed graphs induced by  $\hat{A}_\ell$ 's.

We consider all possible length-2 and length-3 cycles in those graphs, whose indices are as follows:

$$I_{2,\ell} = \{(i, j) : i \neq j, \hat{\alpha}_{ij\ell} > 0, \hat{\alpha}_{jil} > 0\}, \quad \ell \in [\tau],$$

$$I_{3,\ell} = \{(i, j, k) : i, j, k \text{ mutually different}, \hat{\alpha}_{ij\ell} > 0, \hat{\alpha}_{jkl} > 0, \hat{\alpha}_{kil} > 0\}, \quad \ell \in [\tau].$$

Intuitively, in each cycle, the edge with the least weight could be caused by noisy observation, meaning that we should remove such edges to eliminate the corresponding cycle. To do so, we impose the following *data-adaptive linear cycle elimination constraints* to shrink the weights

of those “least important edges”:

$$\begin{aligned}\alpha_{ij\ell} + \alpha_{jil} &\leq \delta_{2,\ell}(i, j), & (i, j) \in I_{2,\ell}, & \ell \in [\tau], \\ \alpha_{ij\ell} + \alpha_{jkl} + \alpha_{kil} &\leq \delta_{3,\ell}(i, j, k), & (i, j, k) \in I_{3,\ell}, & \ell \in [\tau],\end{aligned}\tag{11}$$

where the *data-adaptive regularization strength parameters*  $\delta_{2,\ell}(i, j), \delta_{3,\ell}(i, j, k)$  are defined as follows:

$$\begin{aligned}\delta_{2,\ell}(i, j) &= \hat{\alpha}_{ij\ell} + \hat{\alpha}_{jil} - \min\{\hat{\alpha}_{ij\ell}, \hat{\alpha}_{jil}\} = \max\{\hat{\alpha}_{ij\ell}, \hat{\alpha}_{jil}\}, & (i, j) \in I_{2,\ell}, & \ell \in [\tau], \\ \delta_{3,\ell}(i, j, k) &= \hat{\alpha}_{ij\ell} + \hat{\alpha}_{jkl} + \hat{\alpha}_{kil} - \min\{\hat{\alpha}_{ij\ell}, \hat{\alpha}_{jkl}, \hat{\alpha}_{kil}\}, & (i, j, k) \in I_{3,\ell}, & \ell \in [\tau].\end{aligned}\tag{12}$$

**Remark 3** (Flexibility). One advantage of our data-adaptive linear constraint is its flexibility: In (11), we consider length-2 and length-3 cycles since (i) it is computationally intensive to consider longer cycles and (ii) those less important edges in length-2 and length-3 cycles could also appear in longer cycles, meaning removing them suffices to eliminate longer cycles. However, it is the user’s choice to decide which potential cycle should be included in the constraint. For example, if we additionally include length-1 cycles with data-adaptive regularization strength parameters  $\hat{\alpha}_{iil}$ ’s, we can expect to obtain a strict DAG structure (i.e., without any lagged self-exciting components).

### 3.2 Constrained joint VI-based estimation

Different from the aforementioned decoupled learning approach in Section 2.4, here we need to estimate parameters  $\theta_1, \dots, \theta_{d_1}$  jointly to remove cycles and encourage our desired DAG structure. We concatenate the parameter vectors and response vectors into matrices as follows:

$$\theta = (\theta_1, \dots, \theta_{d_1}) \in \mathbb{R}^{d \times d_1}, \quad Y = (Y_{1:T}^{(1)}, \dots, Y_{1:T}^{(d_1)}) \in \mathbb{R}^{T \times d_1},$$

where  $Y_{1:T}^{(i)}$  is defined in (7). The feasible region of the concatenated parameter is then defined as:

$$\tilde{\Theta} = \{\theta = (\theta_1, \dots, \theta_{d_1}) : \theta_i \in \Theta, i \in [d_1]\}.\tag{13}$$

The joint estimator coupled with the data-adaptive linear cycle elimination constraint is defined as the weak solution to the following Variational Inequality:

$$\text{find } \hat{\theta} \in \Theta^{\text{DAL}} : \langle \text{vec}(F_T(\theta)), \text{vec}(\theta - \hat{\theta}) \rangle \geq 0, \quad \forall \theta \in \Theta^{\text{DAL}}, \quad \text{VI}[F_T, \Theta^{\text{DAL}}]$$



where  $\text{vec}(A)$  is the vector of columns of  $A$  stacked one under the other, the empirical “vector” field is

$$F_T(\theta) = (F_T^{(1)}(\theta_1), \dots, F_T^{(d_1)}(\theta_{d_1})) \in \mathbb{R}^{d \times d_1}, \quad (14)$$

and vector field  $F_T^{(i)}(\theta_i) \in \mathbb{R}^d$  is defined in (10). Moreover, the convex set  $\Theta^{\text{DAL}}$  incorporates the above data-adaptive linear constraints (11) and is defined as follows:

$$\Theta^{\text{DAL}} = \left\{ \theta : \theta \in \tilde{\Theta}, e_{f_{j,\ell},d}^T \theta e_{i,d_1} + e_{f_{i,\ell},d}^T \theta e_{j,d_1} \leq \delta_{2,\ell}(i,j), (i,j) \in I_{2,\ell}, \ell \in [\tau], \right. \\ \left. e_{f_{j,\ell},d}^T \theta e_{i,d_1} + e_{f_{k,\ell},d}^T \theta e_{j,d_1} + e_{f_{i,\ell},d}^T \theta e_{k,d_1} \leq \delta_{3,\ell}(i,j,k), (i,j,k) \in I_{3,\ell}, \ell \in [\tau] \right\},$$

where  $f_{j,\ell} = 1 + d_3 + \tau d_2 + (j-1)\tau + \ell$  such that  $e_{f_{j,\ell},d}^T \theta e_{i,d_1} = \alpha_{ij\ell}$ . The regularization strength parameters  $\delta_{2,\ell}(i,j), \delta_{3,\ell}(i,j,k)$  are defined in (12).

### 3.3 A special example: linear link function

Now, we elaborate on our proposed regularization on a special linear link case. The vector field  $F_T(\theta)$  (14) can be expressed as follows:

$$F_T(\theta) = \frac{1}{T} \mathbf{w}_{1:T} \mathbf{w}_{1:T}^T \theta - \frac{1}{T} \mathbf{w}_{1:T} Y = \mathbb{W}_{1:T} \theta - \frac{1}{T} \mathbf{w}_{1:T} Y,$$

where  $\mathbf{w}_{1:T} \in \mathbb{R}^{d \times T}$  is defined in 7. Similar to the linear model example in Section 2.2, the above vector field is the gradient field of the least square objective, and our proposed estimator  $\text{VI}[F_T, \Theta^{\text{DAL}}]$  boils down to the LS estimator, which solves the following constrained optimization problem:

$$\min_{\theta} \frac{1}{2T} \sum_{i=1}^{d_1} \|\mathbf{w}_{1:T}^T \theta_i - Y_{i,1:T}\|_2^2 = \frac{1}{2T} \|\mathbf{w}_{1:T}^T \theta - Y\|_F^2,$$

$$\text{subject to } \mathbf{0}_T \leq \mathbf{w}_{1:T}^T \theta_i \leq \mathbf{1}_T, \quad i \in [d_1], \quad (15)$$

$$e_{f_{j,\ell},d}^T \theta e_{i,d_1} + e_{f_{i,\ell},d}^T \theta e_{j,d_1} \leq \delta_{2,\ell}(i,j), \quad (i,j) \in I_{2,\ell}, \quad \ell \in [\tau],$$

$$e_{f_{j,\ell},d}^T \theta e_{i,d_1} + e_{f_{k,\ell},d}^T \theta e_{j,d_1} + e_{f_{i,\ell},d}^T \theta e_{k,d_1} \leq \delta_{3,\ell}(i,j,k), \quad (i,j,k) \in I_{3,\ell}, \quad \ell \in [\tau].$$

Similarly, (15) is convex and can be efficiently solved by a well-developed toolkit such as **Mosek**.

In many real applications, including our real data example in Section 6, we only consider triggering effect, meaning that we can replace  $\mathbf{w}_{1:T}^T \theta_i \geq \mathbf{0}_T$  with  $\theta_i \geq \mathbf{0}_d$  as a relaxation. In addition, since the prediction of the  $i$ -th event’s occurrence at time  $t$  is by comparing the estimated probability  $w_{t-\tau:t-1}^T \theta_i$  with a cut-off/threshold selected using the validation dataset,

we can further relax the constraint  $\mathbf{w}_{1:T}^\top \theta_i \leq \mathbf{1}_T$  and treat  $w_{t-\tau:t-1}^\top \theta_i$  as a ‘‘score’’ instead of a probability. Thus, we can adopt the following penalized form:

$$\begin{aligned} \min_{\theta} \quad & \frac{1}{2T} \|\mathbf{w}_{1:T}^\top \theta - Y\|_F^2 + \sum_{\ell=1}^{\tau} \sum_{(i,j) \in I_{2,\ell}} \frac{\lambda}{\delta_{2,\ell}(i,j)} (e_{f_{j,\ell},d}^\top \theta e_{i,d_1} + e_{f_{i,\ell},d}^\top \theta e_{j,d_1}) \\ & + \sum_{\ell=1}^{\tau} \sum_{(i,j,k) \in I_{3,\ell}} \frac{\lambda}{\delta_{3,\ell}(i,j,k)} (e_{f_{j,\ell},d}^\top \theta e_{i,d_1} + e_{f_{k,\ell},d}^\top \theta e_{j,d_1} + e_{f_{i,\ell},d}^\top \theta e_{k,d_1}), \end{aligned}$$

subject to  $\theta_i \geq \mathbf{0}_T$ ,  $i \in [d_1]$ .

(16)

Here,  $\lambda$  is a hyperparameter that controls the strength of regularization. The data-adaptive regularization strength parameter  $\delta_{2,\ell}(i,j)$  (or  $\delta_{3,\ell}(i,j,k)$ ) appears in the denominator since smaller  $\delta_{2,\ell}(i,j)$  (or  $\delta_{3,\ell}(i,j,k)$ ) implies stronger penalty on the corresponding cycle, which closely resembles adaptive Lasso Zou [2006]. Most importantly, (16) can be solved efficiently using PGD, where at each iteration, the update rule is as follows:

$$\begin{aligned} \hat{\theta} \leftarrow \hat{\theta} - \eta \left( F_T(\hat{\theta}) + \sum_{\ell=1}^{\tau} \sum_{(i,j) \in I_{2,\ell}} \frac{\lambda}{\delta_{2,\ell}(i,j)} (e_{f_{j,\ell},d} e_{i,d_1}^\top + e_{f_{i,\ell},d} e_{j,d_1}^\top) \right. \\ \left. + \sum_{\ell=1}^{\tau} \sum_{(i,j,k) \in I_{3,\ell}} \frac{\lambda}{\delta_{3,\ell}(i,j,k)} (e_{f_{j,\ell},d} e_{i,d_1}^\top + e_{f_{k,\ell},d} e_{j,d_1}^\top + e_{f_{i,\ell},d} e_{k,d_1}^\top) \right), \end{aligned} \quad (17)$$

where  $\eta$  is the step size/learning rate hyperparameter and  $F_T(\cdot)$  is the empirical field (14). After the above update in each iteration, the projection onto the feasible region  $\mathbb{R}_+^{d \times d_1}$  can be simply done by replacing all negative entries in  $\hat{\theta}$  with zeros.

### 3.4 Penalized joint VI-based estimation

As previously discussed in Section 2.4, the VI $[F_T^{(i)}, \Theta]$  can be solved by PGD as the feasible region  $\Theta$  is a convex set. However, VI $[F_T, \Theta^{\text{DAL}}]$  additionally incorporates the data-adaptive linear constraints into its feasible region  $\Theta^{\text{DAL}}$  to encourage a DAG structure with desired lagged self-exciting components, making the projection step harder to implement. Alternatively, it will be much easier if we can transfer the constraints into the penalty. Inspired by the penalized form for the linear link special case (16) (which is very similar to adaptive Lasso Zou [2006]), we propose a *data-adaptive linear penalized VI-based estimator*, which is

the weak solution to the following Variational Inequality:

$$\text{find } \hat{\theta} \in \tilde{\Theta} : \langle \text{vec}(F_T^{\text{DAL}}(\theta)), \text{vec}(\theta - \hat{\theta}) \rangle \geq 0, \quad \forall \theta \in \tilde{\Theta}, \quad \text{VI}[F_T^{\text{DAL}}, \tilde{\Theta}]$$

where the feasible region  $\tilde{\Theta}$  is defined in (13) and the *data-adaptive linear penalized vector field*  $F_T^{\text{DAL}}(\theta)$  is defined as follows:

$$\begin{aligned} F_T^{\text{DAL}}(\theta) = F_T(\theta) &+ \sum_{\ell=1}^{\tau} \sum_{(i,j) \in I_{2,\ell}} \frac{\lambda}{\delta_{2,\ell}(i,j)} (e_{f_{j,\ell,d}} e_{i,d_1}^{\text{T}} + e_{f_{i,\ell,d}} e_{j,d_1}^{\text{T}}) \\ &+ \sum_{\ell=1}^{\tau} \sum_{(i,j,k) \in I_{3,\ell}} \frac{\lambda}{\delta_{3,\ell}(i,j,k)} (e_{f_{j,\ell,d}} e_{i,d_1}^{\text{T}} + e_{f_{k,\ell,d}} e_{j,d_1}^{\text{T}} + e_{f_{i,\ell,d}} e_{k,d_1}^{\text{T}}). \end{aligned} \quad (18)$$

Here,  $\lambda$  is a tunable penalty strength hyperparameter,  $F_T(\theta) = (F_T^{(1)}(\theta_1), \dots, F_T^{(d_1)}(\theta_{d_1})) \in \mathbb{R}^{d \times d_1}$  is the concatenated field (14) and vector field  $F_T^{(i)}(\theta_i) \in \mathbb{R}^d$  is defined in (10). Compared with  $\text{VI}[F_T, \Theta^{\text{DAL}}]$ , it is much easier to solve  $\text{VI}[F_T^{\text{DAL}}, \tilde{\Theta}]$  using PGD. For example, in the exponential link function case, if we restrict our consideration to triggering effect only, we can use (17) as the update rule in PGD and zero out all negative entries after each update as the projection step in each iteration.

**Remark 4.** The above idea to transfer constraint into a penalty by adding the penalty's derivative to the empirical vector field opens up possibilities to consider various types of penalties to encourage desired structures when using our proposed VI-based estimator, e.g., the continuous DAG characterization Zheng et al. [2018] and the adaptive Lasso Zou [2006]; one can see Section 5.3 below for more details on our proposed VI-based estimator coupled with DAG regularization (22) and  $\ell_1$  regularization (23).

## 4 Non-asymptotic Performance Guarantee

In this section, we will show our proposed estimator has nice statistical properties, i.e., it is unique and consistent. In addition, we will also derive a linear program (LP) based confidence interval (CI) of parameters  $\theta_i$ 's, which we defer to Appendix B. One pitfall of our theoretical analysis is the lack of guarantee for the proposed data-adaptive linear method and we leave this topic for future discussion. To begin with, we state two necessary model assumptions:

**Assumption 1.** The link function  $g(\cdot)$  is continuous and monotone, and the vector field  $G(\theta) = \mathbb{E}_w[wg(w^{\text{T}}\theta)]$  is well defined (and therefore monotone along with  $g$ ). Moreover,

$g$  is differentiable and has uniformly bounded first order derivative  $m_g \leq |g'| \leq M_g$  for  $0 < m_g \leq M_g$ .

**Assumption 2.** The observations (static, binary, and continuous) are bounded almost surely: there exists  $M_w > 0$  such that at any time step  $t$ , we have  $\|w_{t-\tau:t-1}\|_\infty \leq M_w$  with probability one.

*Consistency of our proposed estimator.* We define an auxiliary vector field

$$\tilde{F}_T^{(i)}(\theta_i) = \frac{1}{T} \sum_{t=1}^T w_{t-\tau:t-1} (g(w_{t-\tau:t-1}^T \theta_i) - g(w_{t-\tau:t-1}^T \theta_i^*)),$$

where  $\theta_i^*$  is the unknown ground truth. This vector field changes the constant term in  $F_T^{(i)}(\theta_i)$  to ensure its unique root/weak solution to corresponding VI is  $\theta_i^*$ . Recall that our proposed estimator  $\hat{\theta}_i$  is the root of  $F_T^{(i)}(\theta_i)$ . In the following, we will bound the difference between  $\hat{\theta}_i$  and  $\theta_i^*$  via the difference between the empirical vector field  $F_T^{(i)}(\theta_i)$  and the auxiliary vector field  $\tilde{F}_T^{(i)}(\theta_i)$ , i.e.,

$$\Delta^{(i)} = F_T^{(i)}(\theta_i) - \tilde{F}_T^{(i)}(\theta_i) = F_T^{(i)}(\theta_i^*).$$

**Proposition 2.** Under Assumptions 1 and 2, for any  $\varepsilon \in (0, 1)$ , with probability at least  $1 - \varepsilon$ ,  $\Delta^{(i)}, i \in [d_1]$ , can be bounded as follows:

$$\|\Delta^{(i)}\|_\infty \leq M_w \sqrt{\log(2d/\varepsilon)/T}. \quad (19)$$

Moreover, this implies

$$\|\Delta^{(i)}\|_2 \leq M_w \sqrt{d \log(2d/\varepsilon)/T}. \quad (20)$$

*Proof.* Denote random vector

$$\xi_t = w_{t-\tau:t-1} \left( g(w_{t-\tau:t-1}^T \theta_i^*) - y_t^{(i)} \right).$$

We can re-write  $\Delta^{(i)} = \sum_{t=1}^T \xi_t / T$ . Define  $\sigma$ -field  $\mathcal{F}_t = \sigma(W_t)$ , and  $\mathcal{F}_0 \subset \mathcal{F}_1 \subset \dots \subset \mathcal{F}_T$  form a filtration. We can show

$$\mathbb{E}[\xi_t | \mathcal{F}_{t-1}] = 0, \quad \text{Var}(\xi_t | \mathcal{F}_{t-1}) = g(w_{t-\tau:t-1}^T \theta_i^*) (1 - g(w_{t-\tau:t-1}^T \theta_i^*)) \leq 1/4.$$

This means  $\xi_t, t \in [T]$ , is a Martingale Difference Sequence. Moreover, its infinity norm is

bounded by  $M_w$  almost surely (Assumption 2). Therefore, by Azuma's inequality, we have

$$\mathbb{P}\left(|\Delta_k^{(i)}| > u\right) \leq 2 \exp\left\{-\frac{u^2}{2TM_w^2}\right\}, \quad k \in [d], \quad \forall u > 0,$$

where  $\Delta_k^{(i)}$  is the  $k$ -th entry of vector  $\Delta^{(i)}$ . By union bound, we have

$$\mathbb{P}\left(|\Delta_k^{(i)}| > u, \quad k = 1, \dots, d\right) \leq 2d \exp\left\{-\frac{u^2}{2TM_w^2}\right\}, \quad \forall u > 0.$$

By setting the RHS of above inequality to  $\varepsilon$  and solving for  $u$ , we prove (19). Besides, since  $\|\Delta\|_2 \leq \sqrt{d}\|\Delta\|_\infty$  holds for any vector  $\Delta \in \mathbb{R}^d$ , we can easily prove (20) using (19).  $\square$

The proof of Proposition 2 leverages the concentration property of martingales. Similar results could also be found in Juditsky et al. [2020], Wei et al. [2021b]. By leveraging this proposition, we can prove the following non-asymptotic estimation error bound:

**Theorem 1** (Upper bound on  $\|\hat{\theta}_i - \theta_i^*\|_2$ ). Under Assumptions 1 and 2, for  $i \in [d_1]$  and any  $\varepsilon \in (0, 1)$ , with probability at least  $1 - \varepsilon$ , the  $\ell_2$  distance between ground truth  $\theta_i^*$  and  $\hat{\theta}_i$ , which is weak solution to  $\text{VI}[F_T^{(i)}, \Theta]$ , can be upper bounded as follows:

$$\|\hat{\theta}_i - \theta_i^*\|_2 \leq \frac{M_w}{m_g \lambda_1} \sqrt{\frac{d \log(2d/\varepsilon)}{T}},$$

where  $\lambda_1$  is the smallest eigenvalue of  $\mathbb{W}_{1:T} = \sum_{t=1}^T w_{t-\tau:t-1} w_{t-\tau:t-1}^\top / T$  (5).

*Proof of Theorem 1.* Under Assumption 1, the vector field  $F_T^{(i)}(\theta_i)$  is monotone modulus  $m_g \lambda_1$ . This can be proved as follows:

$$\begin{aligned} \left(F_T^{(i)}(\theta) - F_T^{(i)}(\theta')\right)^\top (\theta - \theta') &= \frac{1}{T} \sum_{t=1}^T (w_{t-\tau:t-1}^\top \theta - w_{t-\tau:t-1}^\top \theta') (g(w_{t-\tau:t-1}^\top \theta) - g(w_{t-\tau:t-1}^\top \theta')) \\ &\geq m_g \frac{1}{T} \sum_{t=1}^T \|w_{t-\tau:t-1}^\top (\theta - \theta')\|_2^2 \\ &= m_g (\theta - \theta')^\top \frac{1}{T} \sum_{t=1}^T w_{t-\tau:t-1} w_{t-\tau:t-1}^\top (\theta - \theta') \\ &\geq m_g \lambda_1 \|\theta - \theta'\|_2^2. \end{aligned}$$

This gives us

$$\Delta_i^T(\hat{\theta}_i - \theta_i^*) = \left( F_T^{(i)}(\hat{\theta}_i) - F_T^{(i)}(\theta_i^*) \right)^T (\hat{\theta}_i - \theta_i^*) \geq m_g \lambda_1 \|\hat{\theta}_i - \theta_i^*\|_2^2.$$

By triangle inequality, we also have

$$\Delta_i^T(\hat{\theta}_i - \theta_i^*) \leq \|\Delta_i\|_2 \|\hat{\theta}_i - \theta_i^*\|_2.$$

Together with (20) in Proposition 2, we complete the proof.  $\square$

The above theorem is an extension to the general link function case with mixed-type data of Theorem 1 Juditsky et al. [2020]. As pointed out in Juditsky et al. [2020],  $\mathbb{W}_{1:T} \in \mathbb{R}^{d \times d}$  will be full rank when  $T$  is sufficiently large, i.e., with high probability,  $\lambda_1$  will be a positive constant.

**Remark 5** (Identifiability). The uniqueness, or rather, the identifiability, comes from the nice property of the underlying vector field. To be precise, in the proof of the above theorem, we have shown the vector field  $F_T^{(i)}(\theta_i)$  is monotone modulus  $m_g \lambda_1$  under Assumption 1. Then, the following lemma tells us that our proposed estimator is unique:

**Lemma 1** (Lemma 3.1 Juditsky and Nemirovski [2019]). Let  $\Theta$  be a convex compact set and  $H$  be a monotone vector field on  $\Theta$  with monotonicity modulus  $\kappa > 0$ , i.e.,

$$\forall z, z' \in \Theta, [H(z) - H(z')]^T (z - z') \geq \kappa \|z - z'\|_2^2.$$

Then, the weak solution  $\bar{z}$  to  $\text{VI}[H, \Theta]$  exists and is unique. It satisfies:

$$H(z)^T (z - \bar{z}) \geq \kappa \|z - \bar{z}\|_2^2.$$

In the following, we will use both synthetic and real data experiments to show the good performance of our method for causal structural learning.

## 5 Numerical Simulation

In this section, we conduct numerical simulations to show (i) the good performance of VI-based estimator  $\text{VI}[F_T^{(i)}, \Theta]$  compared with other benchmark methods and (ii) the competitive performance of our proposed data-adaptive linear regularization in structural learning over other DAG-inducing regularization approaches.

## 5.1 Evaluation metrics

We consider a simple  $\tau = 1$  case in both experiments, and we are interested in the estimation of model parameters: (i) background intensity  $\nu = (\nu_1, \dots, \nu_{d_1})^\top$  and (ii) self- and mutual-exciting matrix  $A_1 = (\alpha_{ij1})$ ; for brevity, we drop the last subscript “1” and denote the adjacency matrix by  $A = (\alpha_{ij})$ .

*Weight recovery metrics.* We consider (i) the  $\ell_2$  norm of the background intensity estimation error  $\|\hat{\nu} - \nu\|_2$  ( $\nu$  err.) and (ii) matrix  $F$ -norm of the self- and mutual-exciting matrix estimation error  $\|\hat{A} - A\|_F$  ( $A$  err.).

*Structure recovery metrics.* We also report the Structural Hamming Distance (SHD) between  $\hat{A}$  and  $A$ , which reflects how close the recovered graph is to the ground truth. In addition, since we are interested in DAG structure with self-exciting components, we also consider a measure of “DAG-ness” on the recovered adjacency matrix (after zeroing out the diagonal entries of  $\hat{A}$ ), which we denote as  $h(A_0)$ . The definition of  $h(\cdot)$  can be found in (21) later in this section. We need to mention that small  $h(A_0)$  with large SHD means we recover a DAG which is NOT close to the ground truth and this does not imply good structure recovery. Our primary focus is on SHD for structure recovery.

## 5.2 Effectiveness of VI-based estimation

In the first part, we aim to show the good performance of  $\text{VI}[F_T^{(i)}, \Theta]$  by comparing it with various benchmark estimators in terms of weight recovery metrics. The benchmark methods considered here are linear multivariate Hawkes process Wei et al. [2022] and Neural Network (NN) based method Khanna and Tan [2019].

*Experimental setting.* We consider point process data on time horizon  $T = 2000$  generated from a linear MHP with exponential decay kernel. We adopt a uniform decay rate 0.9. The background intensity and the self- and mutual-exciting magnitude are visualized as ground truth in Figure 2. The time series data (which we use to fit the models) are constructed using the number of events observed at discrete time grids  $1, \dots, T$ .

It is important to recognize this setting mimics the real EMR dataset — although the vital signs and Lab results all have their exact occurrence times, they are binned together in an hourly manner. Through this experiment, we aim to show our model can output meaningful results even under the model mis-specification. In addition, this experiment is also used to show why the point process model developed in our prior work Wei et al. [2022] failed to

handle such real-world time series data in terms of prediction.

*Model training.* We use PGD, and the optimization package Mosek ApS [2019] to train the model. As for benchmark procedures, we use the algorithms and the open source implementations in Wei et al. [2022], Khanna and Tan [2019] for MHP and NN methods, respectively. In addition, we fit the ground truth model (i.e., linear MHP with exponential decay) on the original point process data as a sanity check. We defer further training details to Appendix C.1.

*Results.* We visualize the recovered graphs in Figure 2, where the size of the  $i$ -th node is proportional to the background intensity  $\nu_i$  and the width of the (directed) edge from  $j$ -th node to  $i$ -th node is proportional to the triggering effect magnitude  $\alpha_{ij}$ ; we also report quantitative metrics  $\nu$  err. and  $A$  err. in Table 2.

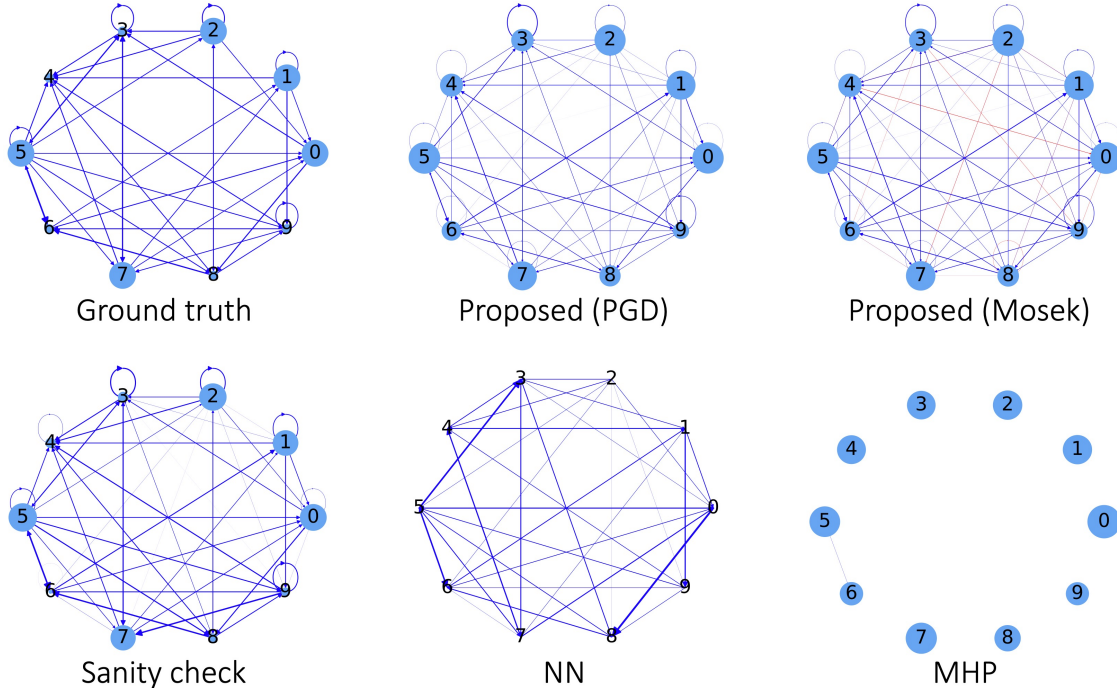


Figure 2: Simulated example: demonstration of the effectiveness of  $\text{VI}[F_T^{(i)}, \Theta]$ . We visualize the recovered (directed) self- and mutual-exciting graph and the background intensity: the size of the node is proportional to the background intensity, and the width of the edge is proportional to the exciting (blue) or inhibiting (red) effect magnitude. The NN-based method does not consider the background intensities and the self-exciting patterns, and MHP fails to recover the interactions among the nodes. In contrast, our proposed model is robust and can faithfully capture the graph structure even under model mis-specification.

The recovered graph structures in Figure 2 demonstrate that our proposed model is capable of estimating the parameters accurately even under model mis-specification and achieves



Table 2: Simulated example: quantitative metrics of the example in Figure 2. We can observe our proposed ( $\text{VI}[F_T^{(i)}, \Theta]$ ) achieves the best results except for the sanity check; the sanity check utilizes the raw point process data to estimate model parameters, whereas the rest of the models only have access to time series data. This example demonstrates the good and robust performance of ( $\text{VI}[F_T^{(i)}, \Theta]$ ) under model mis-specification.

Method	Proposed (PGD)	Proposed (Mosek)	NN	MHP	Sanity check
$\nu$ err.	.264	.286	–	.425	.0452
$A$ err.	.308	.323	.345	.629	.130

the best performance among all benchmarks. This is also supported by the quantitative comparisons in Table 2 — our proposed method has the smallest error among all methods (except the sanity check). While the NN-based approach can capture most of the interactions among events, it does not capture the self-exciting patterns as well as the background intensities at all. There is an interesting finding for the MHP method: Although it can handle time series data, the loss of time granularity when converting raw point process data to time series data makes it unable to capture the true dynamics among the events — it over-estimates the background intensities and fails to capture the interactions among those nodes, even under the correct model specification. In contrast, our proposed discrete-time Hawkes network is much more robust and can recover the true dynamics accurately even under such a lack of granularity, which suggests its usefulness in the real-world EMR dataset.

In addition to the above setting, we also consider time series data generated from our proposed discrete-time Hawkes network as a sanity check. Besides, we show the empirical success of project gradient descent in solving  $\text{VI}[F_T^{(i)}, \Theta]$  with various types of link functions. Due to space consideration, we defer those two experiments to Appendices C.2 and C.3, respectively.

### 5.3 Effectiveness of our data-adaptive linear regularization

In the second part of our numerical simulation, we will compare various types of regularization when there is not a sufficient amount of data. Now, let us formally introduce several benchmark regularization approaches as well as the aforementioned DAG-ness measure as follows:

*Benchmark DAG-inducing regularization.* We consider the following benchmarks:

- i) *Continuous DAG regularization.* We encourage the DAG structure directly using a

recently developed continuous and differentiable (but not convex) characterization Zheng et al. [2018]. Recall that we use  $A = (\alpha_{ij})$  to denote  $A_1 = (\alpha_{ij1})$  in  $\tau = 1$  case for brevity. The DAG characterization is given by:

$$h(A) = \text{tr}(e^A) - d. \quad (21)$$

For  $A \in \mathbb{R}_+^{d_1 \times d_1}$ , we have  $h(A) \geq 0$ , and  $h(A) = 0$  iff the directed graph induced by  $A$  is a DAG. Therefore,  $h(A)$  can measure the DAG-ness of  $A$ . Most importantly, this DAG characterization has closed form derivative as follows:

$$\nabla h(A) = (e^A)^T.$$

Inspired by Ng et al. [2020], we use this characterization as a penalty directly. We take advantage of its differentiability and add its derivative to the concatenated field  $F_T(\theta)$  (14), which will be treated as the gradient field in PGD. More specifically, let  $J = (\mathbf{0}_{d_1}, I_{d_1}) \in \mathbb{R}^{d_1 \times d}$  and we will have  $J\theta = A^T$ . Then, the vector field coupled with DAG regularization  $F_T^{\text{DAG}}(\cdot)$  is defined as follows:

$$F_T^{\text{DAG}}(\theta) = F_T(\theta) + \lambda J^T \nabla h(J\theta) = F_T(\theta) + \lambda J^T e^A, \quad (22)$$

where tunable hyperparameter  $\lambda$  controls the penalty strength. The PGD update rule is given by:

$$\hat{\theta} \leftarrow \hat{\theta} - \eta F_T^{\text{DAG}}(\hat{\theta}),$$

where  $\eta$  is the step size/learning rate hyperparameter and also tunable.

- ii) *A proposed variant of DAG regularization.* One drawback of the aforementioned DAG regularization is that it removes not only cycles but also lagged self-exciting components; this is evidenced in Figure 3. To keep those informative lagged self-exciting components, we simply zero out the diagonal elements in DAG regularization derivative  $\nabla h(J\theta)$  in (22). Thus, the PGD update will not shrink the diagonal elements.
- iii)  *$\ell_1$  regularization.* We adopt the  $\ell_1$  penalty as another benchmark, which encourages a sparse graph structure and, in turn, eliminates cycles. The  $\ell_1$  penalized vector field is defined as follows:

$$F_T^{\ell_1}(\theta) = F_T(\theta) + \lambda J^T \nabla (|J\theta|_1), \quad (23)$$

where  $|\cdot|_1$  is the summation of the absolute values of all entries. Similarly, the VI-based estimator can be efficiently solved by PGD using the following update rule:

$$\hat{\theta} \leftarrow \hat{\theta} - \eta F_T^{\ell_1}(\hat{\theta}).$$

- iv) *Adaptive Lasso*. As a variant of  $\ell_1$  regularization, adaptive  $\ell_1$  regularization (or adaptive Lasso Zou [2006]) replaces  $\lambda|\alpha_{ij}|$  with  $\frac{\lambda}{\hat{\alpha}_{ij}}|\alpha_{ij}|$  in (23); for  $\hat{\alpha}_{ij} = 0$  case, we adopt a simple remedy by adding penalty term  $10^3\lambda|\alpha_{ij}|$  to enforce  $\alpha_{ij}$  to be zero.

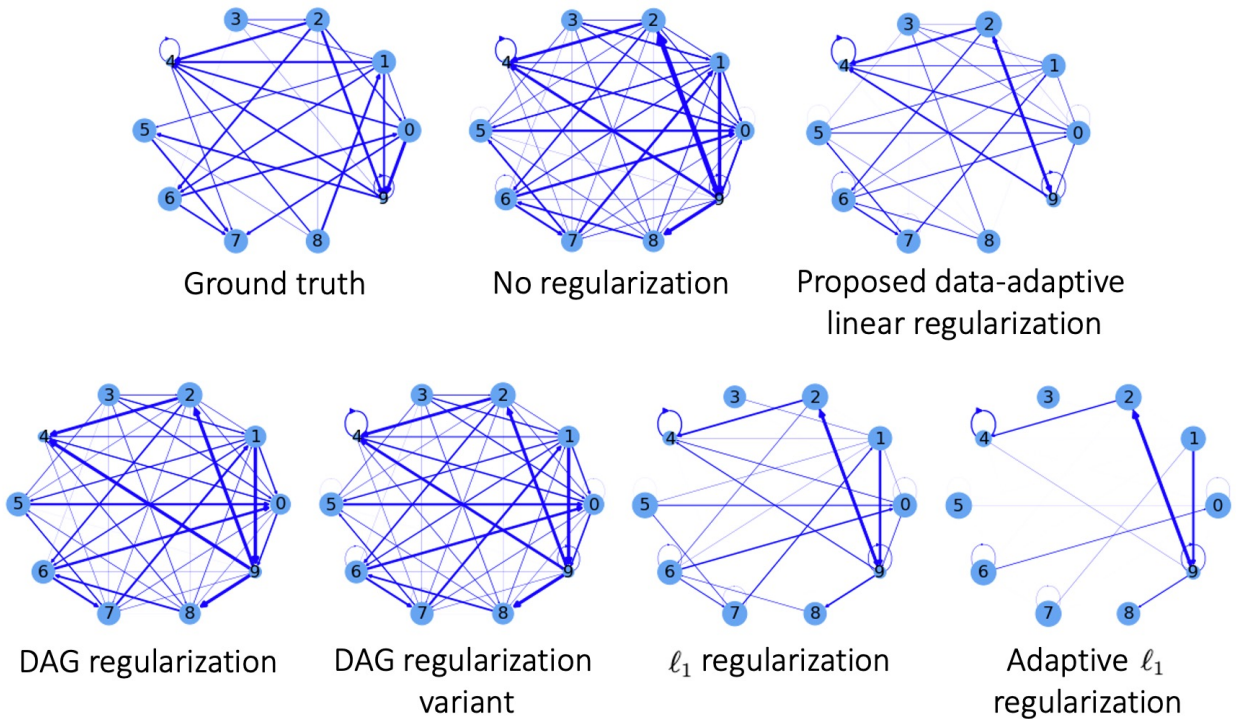


Figure 3: Simulated example: demonstration of the effectiveness of our proposed data-adaptive linear regularization. We visualize the recovered graph structures for a  $d_1 = 10$  and  $T = 500$  illustrative example using our proposed VI-based estimator coupled with various types of regularization (specified on top of each panel). We can observe that our proposed VI-based estimator coupled with our proposed data-adaptive linear constraint can return the closest graph structure to the ground truth; see quantitative evaluation metrics, such as SHD, in Table 3.

*Results.* We first demonstrate the competitive performance of our proposed data-adaptive linear method on a  $d_1 = 10$  illustrative example, where we adopt an exponential link function and the true graph structure is visualized in the top left panel in Figure 3. The complete

Table 3: Simulated example: quantitative metrics of the example in Figure 3. We can observe that our proposed VI-based estimator, coupled with our proposed data-adaptive linear constraint, can achieve better estimation accuracy while encouraging a desired DAG structure. Besides, our proposed method also gives the best structure recovery, i.e., the smallest SHD; although the adaptive  $\ell_1$  approach achieves the best DAG-ness, it achieves so by removing many important edges and cannot output a correct graph structure (as evidenced in Figure 3).

Regularization	None	Proposed	DAG	DAG-Variant	$\ell_1$	Ada. $\ell_1$
$A$ err.	.3874	<b>.2094</b>	.3541	.2949	.2501	.3022
$\nu$ err.	.1175	<b>.0775</b>	.0895	.0841	.0884	.1251
$h(A_0)$	.1223	.0308	.0337	.0242	.0274	<b>.0232</b>
SHD	41	<b>25</b>	32	34	41	29

details, e.g., random DAG generation and PGD to solve for the estimators, are deferred to Appendix C.4, and we only report results here. We visualize the recovered graphs using our VI-based estimator with exponential link coupled with various types of regularization in Figure 3, and we report all aforementioned quantitative metrics in Table 3. We observe that our proposed data-adaptive linear regularization can achieve the best weight recovery accuracy (in terms of  $\nu$  err. and  $A$  err.) and structure recovery accuracy (in terms of SHD) compared with all benchmark methods.

To further validate the good performance of our proposed data-adaptive linear method, we run 100 independent trials for  $d_1 = 10, T = 500$  and  $d_1 = 20, T = 1000$  cases as well as linear link and exponential link functions cases. We plot the mean and standard deviation of  $A$  err. and SHD in Figure 4; for completeness, we also report the raw values of the mean and standard deviation of all four aforementioned metrics in Table 9 in Appendix C.4.

Figure 4 shows that, in low dimensional (i.e.,  $d_1 = 10$ ) case,  $\ell_1$  regularization does well in weight recovery but fails in structure recovery, whereas our proposed variant of DAG regularization prioritizes the structure recovery but performs poorly in weight recovery. As a comparison, our proposed data-adaptive linear regularization achieves comparable weight and structure recovery accuracy to  $\ell_1$  regularization and the proposed variant of DAG regularization, respectively, suggesting that it can balance the weight recovery accuracy and the structure recovery accuracy in low dimensional case.

In higher dimensional (i.e.,  $d_1 = 20$ ) case, our proposed approach achieves the best structure recovery accuracy (i.e., the smallest SHD) while maintaining nearly the same weight recovery accuracy with the best result (achieved by  $\ell_1$  regularization-based method).

It is interesting to observe that adaptive  $\ell_1$  regularization’s performance lies between  $\ell_1$  regularization and our proposed regularization. In addition, our proposed regularization has a dominating performance over DAG regularization-based approaches in terms of both structure recovery accuracy and weight recovery accuracy. These observations are also validated by Table 9 in the appendix.

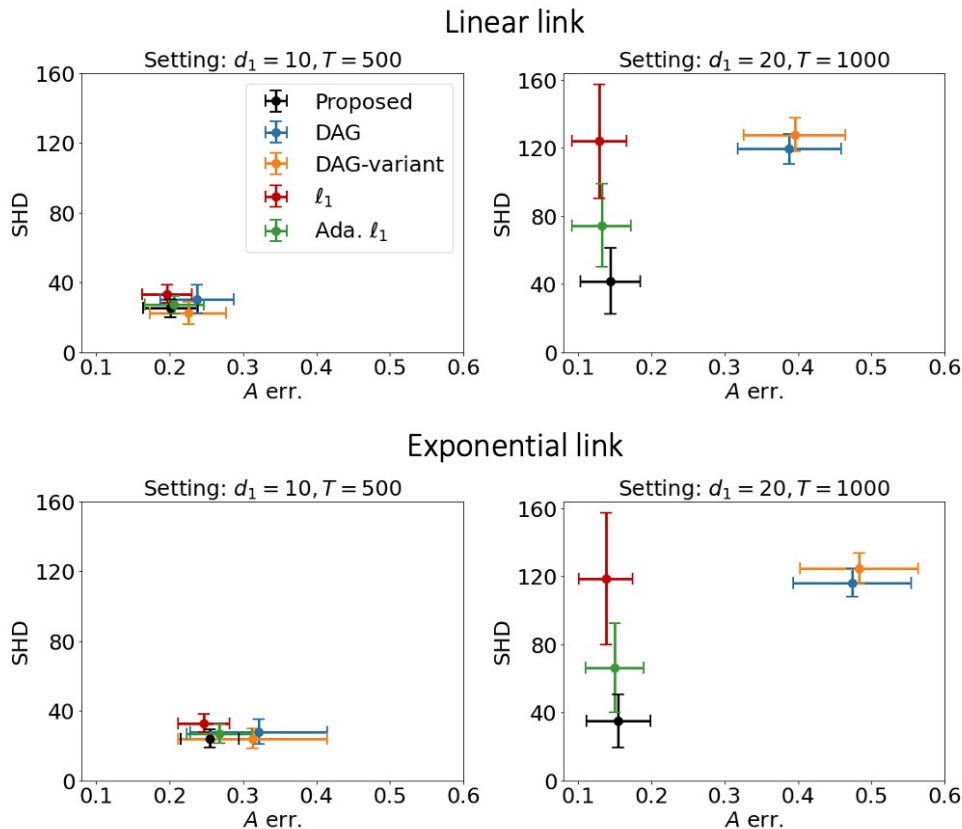


Figure 4: Simulation: mean (dot) and standard deviation (error bar) of matrix  $F$ -norm of the self- and mutual-exciting matrix estimation error ( $A$  err.) and Structural Hamming Distance (SHD) over 100 independent trials for various types of regularization. For each regularization, the closer it is to the origin, the better it is. We can observe that our proposed data-adaptive linear regularization performs the best (especially in higher dimensional cases) in terms of structure recovery while achieving almost the same weight recovery accuracy with the best result.

Lastly, from Table 9, it is not surprising to observe that the DAG regularization-based approaches do shrink  $h(A_0)$  but fail to return an accurate graph structure (in terms of SHD); it is also not unexpected that adaptive  $\ell_1$  approach achieves the smallest  $h(A_0)$ , since it is designed to output a highly-sparse graph which in turn eliminates all cycles (the bottom right penal in Figure 3). Overall, our proposed regularization achieves the best structural learning

result in terms of SHD, and a very close weight recovery result to  $\ell_1$  approach, suggesting its superior empirical performance over the aforementioned benchmarks.

## 6 Real Data Example

Here, we demonstrate the usefulness of our proposed method on a real study described in Section 1.1.

### 6.1 Sepsis Associated Derangements

We consider in total 6 vital signs and 33 Lab results. To handle such high dimensional information and reduce the complexity of the computations, expert (i.e., clinician) opinion is utilized to identify common and clinically relevant Sepsis Associated Derangements that could be detected using structured EMR data. A SAD is considered present if the corresponding measurements are outside of normal limits, which are determined jointly by already established criteria ABIM and expert opinions; see Table 4 for details. In Table 4, the measurement names explain themselves, and we do not give further descriptions of those measurements. In our previous study Wei et al. [2021a, 2022], the constructed SADs were shown to be appropriate by the fact that the Sepsis-3 cohort demonstrated a closer relationship with the SADs than the Non-Septic cohort and other real-data results therein. Here, our goal is to demonstrate that our proposed model can recover an explainable graph structure of those SADs while maintaining prediction accuracy.

### 6.2 Evaluation metrics

Since we do not have the ground truth anymore, we use the out-of-sample prediction accuracy, or rather, Area Under the Receiver Operating Characteristic (AUROC), as the major performance evaluation metric; we also consider Area Under the Precision-Recall curve (AUPRC), f1 score and f2 score as additional metrics. Furthermore, we focus on the interpretability of the resulting Granger causal DAG by (i) counting the number of undesirable length- $L$  cycles,  $L \in \{2, 3, 4, 5\}$ , and (ii) studying whether or not the inferred interactions align with well-known physiologic relationships.

Table 4: SAD construction based on thresholding observed vital signs and Lab results via medical knowledge. In our study, we incorporate in total 39 patient features, including 33 Lab results and 6 vital signs.

Full SAD name	Abbreviation	Type	Measurement name	Abnormal threshold
<b>Renal Dysfunction</b>	RenDys	Lab	creatinine	> 1.3
			blood_urea_nitrogen_(bun)	> 20
<b>Electrolyte Imbalance</b>	LyteImbal	Lab	calcium	> 10.5
			chloride	< 98 or > 106
			magnesium	< 1.6
			potassium	> 5.0
			phosphorus	> 4.5
<b>Oxygen Transport Deficiency</b>	O2TxpDef	Lab	hemoglobin	< 12
<b>Coagulopathy</b>	Coag	Lab	partial_prothrombin_time_(ptt)	> 35
			fibrinogen	< 233
			platelets	< 150000
			d_dimer	> 0.5
			thrombin_time	> 20
			prothrombin_time_(pt)	> 13
			inr	> 1.5
<b>Malnutrition</b>	MalNut	Lab	transferrin	< 0.16
			prealbumin	< 16
			albumin	< 3.3
<b>Cholestasis</b>	Chole	Lab	bilirubin_direct	> 0.3
			bilirubin_total	> 1.0
<b>Hepatocellular Injury</b>	HepatoDys	Lab	aspartate_aminotransferase_(ast)	> 40
			alanine_aminotransferase_(alt)	> 40
			ammonia	> 70
<b>Acidosis</b>	Acidosis	Lab	base_excess	< -3
			ph	< 7.32
<b>Leukocyte Dysfunction</b>	LeukDys	Lab	white_blood_cell_count	< 4 or > 12
<b>Hypercarbia</b>	HypCarb	Lab	end_tidal_co2	> 45
			partial_pressure_of_carbon_dioxide_(paco2)	> 45
<b>Hyperglycemia</b>	HypGly	Lab	glucose	> 125
<b>Myocardial Ischemia</b>	MyoIsch	Lab	troponin	> 0.04
<b>Oxygen Diffusion Dysfunction (Lab results)</b>	O2DiffDys (L)	Lab	saturation_of_oxygen_(sao2)	< 92
<b>Diminished Cardiac Output (Lab results)</b>	DCO (L)	Lab	b-type_natriuretic_peptide_(bnp)	> 100
<b>Tissue Ischemia</b>	TissueIsch	Lab	base_excess	< -3
			lactic_acid	> 2.0
<b>Diminished Cardiac Output (vital signs)</b>	DCO (V)	Vital signs	best_map	< 65
<b>CNS Dysfunction</b>	CNSDys	Vital signs	gcs_total_score	< 14
<b>Oxygen Diffusion Dysfunction (vital signs)</b>	O2DiffDys (V)	Vital signs	spo2	< 92
			fio2	> 21
<b>Thermoregulation Dysfunction</b>	ThermoDys	Vital signs	temperature	< 36 or > 38
<b>Tachycardia</b>	Tachy	Vital signs	pulse	> 90

### 6.3 Model comparison

*Candidate models.* We compare the VI-based estimation  $\text{VI}[F_T^{(i)}, \Theta]$  with the black-box methods — we choose XGBoost over other models, e.g., Neural Networks, since it outperformed other candidate models in the sepsis prediction challenge Reyna et al. [2020]. As for  $\text{VI}[F_T^{(i)}, \Theta]$ , we consider linear and sigmoid link functions; furthermore, for linear link case, we consider model training with and without prior medical knowledge that no inhibiting effect exists by using PGD and Mosek, respectively.

*Results.* We fit those aforementioned candidate models to the real data in the year 2018. To quantitatively compare those models, we calculate the in-sample Area Under the Receiver Operating Characteristic using the training data (the year 2018) and the out-of-sample AUROC using testing data (the year 2019) for each SAD as the response variable. We report the in-sample and the out-of-sample AUROCs in Table 5.

From Table 5, we can observe that our proposed model with linear link function achieves the best performance for predicting most SADs. Although the sigmoid link function seems a better choice in some cases, the improvement compared to the linear link function is marginal, except for predicting Oxygen Diffusion Dysfunction (Lab results). XGBoost, as a black-box algorithm, does achieve great performance in the 2018 training data but fails to generalize to 2019 testing data, i.e., its out-of-sample AUROCs are much smaller than the in-sample ones for nearly all cases. We need to remark that selecting hyperparameters from finer grids may lead to better out-of-sample performance for XGBoost, but such a grid search approach is too time-consuming since there are too many hyperparameters to tune, and the results remain inexplicable.

In addition to the quantitative comparison, we visualize the recovered Granger causal graphs of the SADs in Figure 11 in Appendix D.1, which demonstrates the usefulness of prior medical knowledge in outputting a sparse and interpretable graph structure. Due to space consideration, we defer more findings, interpretations, and complete model training details to Appendix D.1.

### 6.4 Uncertainty quantification

Previous model comparison results in Table 5 show the competitive performance of our proposed method with the linear link function. In this subsection, we will adopt this model and use PGD to learn the model parameters. Most importantly, we aim to explore various regularizations to enhance interpretability. We will perform train-validation-test data split



Table 5: Comparison of AUROCs for our proposed method with linear link function, Sigmoid link function, and the benchmark XGBoost method. For our proposed method with linear link function, we use Mosek and PGD to obtain our proposed estimator. We report the in-sample AUROC using the training data (the year 2018) and the out-of-sample AUROC using testing data (the year 2019). The best out-of-sample AUROCs are highlighted. We can observe  $VI[F_T^{(i)}, \Theta]$  coupled with linear link achieves the best out-of-sample prediction accuracy for most SADs.

Resp. SAD Abbrev.	Linear (Mosek)		Linear (PGD)		Sigmoid		XGBoost	
	2018	2019	2018	2019	2018	2019	2018	2019
RenDys	.642	.607	.596	.586	.650	<b>.608</b>	.612	.543
LyteImbal	.617	<b>.602</b>	.594	.569	.612	.592	.628	.522
O2TxpDef	.655	<b>.639</b>	.649	.634	.657	.637	.660	.538
DCO (L)	.763	<b>.692</b>	.743	.669	.645	.500	.500	.500
DCO (V)	.838	<b>.805</b>	.823	.796	.837	.801	.812	.726
CNSDys	.964	<b>.968</b>	.961	.965	.964	.967	.936	.945
Coag	.596	.566	.542	.519	.600	<b>.576</b>	.612	.558
MalNut	.641	.612	.620	.604	.632	<b>.615</b>	.609	.530
Chole	.638	.571	.633	.570	.647	<b>.573</b>	.574	.502
HepatoDys	.622	<b>.658</b>	.587	.635	.614	.649	.516	.500
O2DiffDys (L)	.870	.729	.849	.795	.809	<b>.903</b>	.500	.500
O2DiffDys (V)	.830	<b>.795</b>	.829	<b>.795</b>	.828	.778	.870	.680
Acidosis	.771	.796	.773	<b>.800</b>	.773	.786	.648	.521
ThermoDys	.982	<b>.999</b>	.987	<b>.999</b>	.989	<b>.999</b>	.649	.452
Tachy	.921	<b>.916</b>	.920	<b>.916</b>	.921	.914	.843	.830
LeukDys	.639	.604	.613	.590	.635	<b>.617</b>	.623	.520
HypCarb	.752	.780	.744	<b>.788</b>	.741	.734	.634	.516
HypGly	.735	<b>.722</b>	.731	.717	.739	<b>.722</b>	.701	.602
MyoIsch	.787	.712	.765	<b>.723</b>	.725	.659	.614	.529
TissueIsch	.775	<b>.784</b>	.775	<b>.784</b>	.759	.778	.690	.542
Sepsis	.653	<b>.641</b>	.632	.626	.658	.637	.673	.566

to fine-tune the hyperparameters: we still use the 2018 data as the training dataset, and we randomly split the 2019 dataset by half (for both sepsis and non-sepsis patient cohorts) into validation and testing datasets; we will select the hyperparameters based on the model performance on the validation dataset and demonstrate its performance on the test dataset. Here, we perform a grid search to find the best learning rate and total iteration number hyperparameters. We report the resulting graph structure in the left panel of Figure 5. We can use the above method, the vanilla approach in the following, and report the evaluation metrics on the test dataset in the first column of Table 6. Complete details of this hyperparameter selection procedure can be found in Appendix D.2.

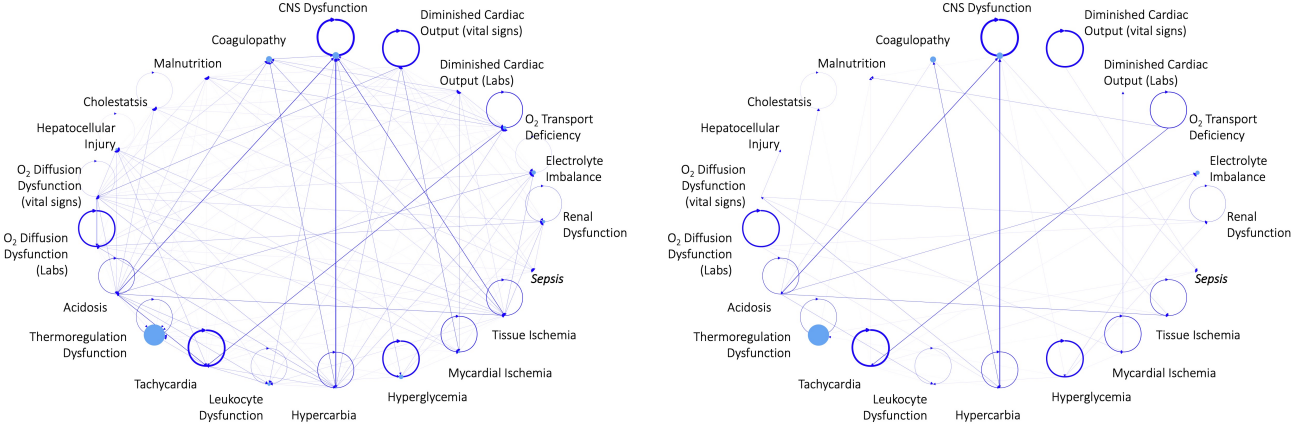


Figure 5: Granger causal graphs recovered by our proposed discrete-time Hawkes network using a linear link with (right) and without (left) bootstrap uncertainty quantification. Here, we use PGD to learn the model parameters. The difference between the left panel here from the top left panel in Figure 11 is that we fine-tune the learning rate and total iteration number hyperparameters. Compared with Figure 11, we observe that bootstrap uncertainty quantification can help remove many edges and enhance result interpretability.

*Directed cycles.* As mentioned in Section 3, cycles (with lengths greater than or equal to two) are undesirable, and we want to remove them to improve result interpretability. Here, we report the number of length- $L$  cycles for  $L \in \{2, 3, 4, 5\}$  in Table 6. As we can see from that table, there are many cycles in the graph recovered by the vanilla approach, making the results less explainable.

*Uncertainty quantification via bootstrap.* In the left panel of Figure 5, we identify many edges with very small magnitudes/weights, making it difficult to determine if the existence of such an edge is the result of noisy observations. For example, although the edge from Diminished Cardiac Output (vital signs) to sepsis events agrees with the well-known causal relationships in sepsis-related illness, its magnitude is too small to convince the clinician that such a

Table 6: Comparison of the quantitative evaluation metrics on testing data among (i) Vanilla (i.e., no bootstrap and no regularization), (ii) bootstrap (BP), (iii) BP coupled with our proposed data-adaptive linear cycle elimination regularization (BP-Proposed), (iv) BP coupled with continuous DAG regularization (BP-DAG) and (v) our proposed variant of DAG regularization to maintain lagged self-exciting components (BP-DAG-variant) as well as (vi) BP coupled with  $\ell_1$  regularization (BP- $\ell_1$ ). We can observe that our proposed regularization does almost the best in improving out-of-sample prediction accuracy in terms of all metrics.

Method	Vanilla	BP	BP-Proposed	BP-DAG	BP-DAG-variant	BP- $\ell_1$
AUROC	.9374 <sub>(.0605)</sub>	.9297 <sub>(.0612)</sub>	<b>.9397</b> <sub>(.0571)</sub>	.9314 <sub>(.0604)</sub>	.9307 <sub>(.0606)</sub>	<b>.9397</b> <sub>(.0556)</sub>
AUPRC	.8514 <sub>(.1154)</sub>	.8521 <sub>(.1062)</sub>	<b>.8545</b> <sub>(.1076)</sub>	.8415 <sub>(.1087)</sub>	.8530 <sub>(.1063)</sub>	.8533 <sub>(.1076)</sub>
f1 score	.8126 <sub>(.1309)</sub>	<b>.8146</b> <sub>(.1198)</sub>	.8139 <sub>(.1207)</sub>	.8050 <sub>(.1243)</sub>	.8143 <sub>(.1200)</sub>	.8139 <sub>(.1207)</sub>
f2 score	.7899 <sub>(.1339)</sub>	.7926 <sub>(.1249)</sub>	.7916 <sub>(.1182)</sub>	.7738 <sub>(.1327)</sub>	.7929 <sub>(.1249)</sub>	<b>.7933</b> <sub>(.1256)</sub>
Len-2 cycle	39	3	0	0	0	0
Len-3 cycle	136	0	0	0	0	0
Len-4 cycle	680	1	0	0	0	0
Len-5 cycle	3310	0	0	0	0	0

triggering effect is statistically significant.

To address this issue, we perform uncertainty quantification via bootstrap. We determine the existence of an edge in the graph based on the 95% bootstrap confidence interval, i.e., we assign zero weight to that edge if the CI contains zero; otherwise, we use the median of the bootstrap results as the weight. The resulting graph is reported in the right panel of Figure 5; in addition, we refer to this bootstrap method as BP and report its quantitative evaluation performance on the test dataset in the second column of Table 6. Complete details on how we obtain these graphs are deferred to Appendix D.2.

By comparing both panels in Figure 5 as well as the results in Table 6, the effect of uncertainty quantification becomes evident — the number of cycles drops drastically while the quantitative performance measures remain nearly unchanged, meaning that those removed edges have a very small impact on the model performance. By removing those “meaningless” edges, we can improve the interpretability. For completeness, we also perform uncertainty quantification for the graph recovered by the Mosek package in the top right panel of Figure 11. We report the results in Figure 12 in Appendix D.2, where we can observe that many unexpected inhibitory relationships disappear. This further validates the usefulness of uncertainty quantification.

However, as shown in Table 6, there are still cycles after the bootstrap uncertainty quantification. To completely remove those cycles, we consider causal structural learning via

our penalized VI-based estimation such as  $\text{VI}[F_T^{\text{DAL}}, \tilde{\Theta}]$ .

## 6.5 Causal DAG recovery via regularization

We adopt the regularization approaches described in Section 3.1 and Section 5.3, and select the regularization hyperparameter  $\lambda$  using grid search; again, for each regularization, we perform bootstrap uncertainty quantification with 1500 trials and 95% confidence level. We report the performance metrics on both validation and testing datasets for each regularization in Table 7. The hyperparameter is selected based on the validation AUROC, and the selected parameters for each regularization method are highlighted in Table 7. The resulting graphs (which correspond to the selected hyperparameters) are visualized at the beginning of this paper in Figure 1. In addition, we summarize the performance metrics on the testing dataset for each regularization (with the corresponding selected hyperparameter) in Table 6.

From Table 6, we can observe that our proposed data-adaptive linear regularization can not only remove cycles while keeping the lagged self-exciting components but also improve the out-of-sample prediction accuracy. In addition, Table 7 shows that our proposed data-adaptive linear regularization can eliminate cycles the most efficiently, i.e., it can remove all the cycles even when the regularization strength is not very strong. Although the continuous DAG regularization can also remove cycles, it cannot keep the informative lagged self-exciting components (as evidenced by the top right penal in Figure 1). Fortunately, our proposed variant can fix this issue and return a graph without cycles but with lagged self-exciting components. However, both DAG regularization-based approaches cannot achieve comparable prediction performance with our proposed linear regularization. Lastly,  $\ell_1$  regularization can “create” more cycles (as evidenced by  $\lambda = 0.0001$  case); although we can see there is no cycle left when  $\lambda$  becomes as large as 0.001, the resulting graph, i.e., the bottom left panel in Figure 1, shows that  $\ell_1$  regularization removes all edges, leading to a very uninformative graph. That is to say, although  $\ell_1$  regularization is capable of encouraging sparse structure, it cannot output a meaningful DAG without removing all edges, which explains why it achieves the best f2 score in Table 6 —  $\ell_1$  regularization removes all edges in the graph, but over-estimates the background intensities, which results in less false negatives, larger recall and therefore larger f2 score (since f2 score weights recall more than precision).

Table 7: Comparison of the quantitative evaluation metrics for different structural learning regularization strength hyperparameters  $\lambda$ 's. We select  $\lambda$  based on the AUROC on the validation dataset, and the selected  $\lambda$  is highlighted for each regularization.

Proposed data-adaptive linear cycle elimination regularization.												
Hyperparameter $\lambda$	0	$10^{-6}$	$5 \times 10^{-6}$	$10^{-5}$	$5 \times 10^{-5}$	$10^{-4}$	<b><math>10^{-3}</math></b>	$10^{-2}$	$10^{-1}$	1	10	
AUROC	Validation	.9274 <sub>(.0656)</sub>	.9271 <sub>(.0660)</sub>	.9272 <sub>(.0671)</sub>	.9338 <sub>(.0645)</sub>	.9366 <sub>(.0625)</sub>	.9366 <sub>(.0623)</sub>	.9379 <sub>(.0601)</sub>	.9379 <sub>(.0601)</sub>	.9379 <sub>(.0601)</sub>	.9379 <sub>(.0601)</sub>	.9379 <sub>(.0601)</sub>
	Testing	.9297 <sub>(.0612)</sub>	.9293 <sub>(.0624)</sub>	.9290 <sub>(.0644)</sub>	.9362 <sub>(.0619)</sub>	.9384 <sub>(.0589)</sub>	.9384 <sub>(.0587)</sub>	.9397 <sub>(.0571)</sub>	.9397 <sub>(.0571)</sub>	.9397 <sub>(.0571)</sub>	.9397 <sub>(.0571)</sub>	.9397 <sub>(.0571)</sub>
AUPRC	Validation	.8496 <sub>(.1161)</sub>	.8496 <sub>(.1160)</sub>	.8494 <sub>(.1166)</sub>	.8513 <sub>(.1158)</sub>	.8523 <sub>(.1161)</sub>	.8525 <sub>(.1159)</sub>	.8527 <sub>(.1157)</sub>	.8527 <sub>(.1157)</sub>	.8527 <sub>(.1157)</sub>	.8527 <sub>(.1157)</sub>	.8527 <sub>(.1157)</sub>
	Testing	.8521 <sub>(.1062)</sub>	.8521 <sub>(.1064)</sub>	.8515 <sub>(.1074)</sub>	.8537 <sub>(.1068)</sub>	.8540 <sub>(.1061)</sub>	.8541 <sub>(.1078)</sub>	.8545 <sub>(.1076)</sub>	.8545 <sub>(.1076)</sub>	.8545 <sub>(.1076)</sub>	.8545 <sub>(.1076)</sub>	.8545 <sub>(.1076)</sub>
f1 score	Validation	.8141 <sub>(.1301)</sub>	.8143 <sub>(.1309)</sub>	.8135 <sub>(.1306)</sub>	.8128 <sub>(.1310)</sub>	.8117 <sub>(.1327)</sub>	.8134 <sub>(.1321)</sub>	.8134 <sub>(.1321)</sub>	.8134 <sub>(.1321)</sub>	.8134 <sub>(.1321)</sub>	.8134 <sub>(.1321)</sub>	.8134 <sub>(.1321)</sub>
	Testing	.8146 <sub>(.1198)</sub>	.8146 <sub>(.1196)</sub>	.8140 <sub>(.1201)</sub>	.8133 <sub>(.1201)</sub>	.8126 <sub>(.1214)</sub>	.8139 <sub>(.1207)</sub>	.8139 <sub>(.1207)</sub>	.8139 <sub>(.1207)</sub>	.8139 <sub>(.1207)</sub>	.8139 <sub>(.1207)</sub>	.8139 <sub>(.1207)</sub>
f2 score	Validation	.7892 <sub>(.1381)</sub>	.7893 <sub>(.1381)</sub>	.7886 <sub>(.1378)</sub>	.7886 <sub>(.1378)</sub>	.7891 <sub>(.1314)</sub>	.7892 <sub>(.1313)</sub>	.7892 <sub>(.1313)</sub>	.7892 <sub>(.1313)</sub>	.7892 <sub>(.1313)</sub>	.7892 <sub>(.1313)</sub>	.7892 <sub>(.1313)</sub>
	Testing	.7926 <sub>(.1249)</sub>	.7924 <sub>(.1253)</sub>	.7926 <sub>(.1252)</sub>	.7925 <sub>(.1251)</sub>	.7911 <sub>(.1180)</sub>	.7916 <sub>(.1182)</sub>	.7916 <sub>(.1182)</sub>	.7916 <sub>(.1182)</sub>	.7916 <sub>(.1182)</sub>	.7916 <sub>(.1182)</sub>	.7916 <sub>(.1182)</sub>
Num. of Len-2 cycles	3	2	1	0	0	0	0	0	0	0	0	
Num. of Len-3 cycles	0	0	0	0	0	0	0	0	0	0	0	
Num. of Len-4 cycles	1	0	0	0	0	0	0	0	0	0	0	
Num. of Len-5 cycles	0	0	0	0	0	0	0	0	0	0	0	

Continuous DAG regularization.												
Hyperparameter $\lambda$	0	$10^{-6}$	$5 \times 10^{-6}$	$10^{-5}$	$5 \times 10^{-5}$	$10^{-4}$	$10^{-3}$	$10^{-2}$	$10^{-1}$	1	10	
AUROC	Validation	.9274 <sub>(.0656)</sub>	.9274 <sub>(.0657)</sub>	.9275 <sub>(.0656)</sub>	.9274 <sub>(.0656)</sub>	.9273 <sub>(.0660)</sub>	.9270 <sub>(.0663)</sub>	.9256 <sub>(.0673)</sub>	.9127 <sub>(.0794)</sub>	.9287 <sub>(.0678)</sub>	.9258 <sub>(.0680)</sub>	.9233 <sub>(.0708)</sub>
	Testing	.9297 <sub>(.0612)</sub>	.9297 <sub>(.0612)</sub>	.9297 <sub>(.0612)</sub>	.9297 <sub>(.0612)</sub>	.9297 <sub>(.0615)</sub>	.9295 <sub>(.0615)</sub>	.9276 <sub>(.0626)</sub>	.9157 <sub>(.0727)</sub>	.9314 <sub>(.0604)</sub>	.9282 <sub>(.0614)</sub>	.9264 <sub>(.0611)</sub>
AUPRC	Validation	.8496 <sub>(.1161)</sub>	.8496 <sub>(.1161)</sub>	.8496 <sub>(.1161)</sub>	.8496 <sub>(.1161)</sub>	.8496 <sub>(.1163)</sub>	.8495 <sub>(.1162)</sub>	.8482 <sub>(.1167)</sub>	.8355 <sub>(.1245)</sub>	.8396 <sub>(.1214)</sub>	.8158 <sub>(.1256)</sub>	.8152 <sub>(.1256)</sub>
	Testing	.8521 <sub>(.1062)</sub>	.8522 <sub>(.1062)</sub>	.8522 <sub>(.1062)</sub>	.8521 <sub>(.1063)</sub>	.8520 <sub>(.1065)</sub>	.8519 <sub>(.1063)</sub>	.8505 <sub>(.1075)</sub>	.8382 <sub>(.1122)</sub>	.8415 <sub>(.1087)</sub>	.8192 <sub>(.1136)</sub>	.8189 <sub>(.1129)</sub>
f1 score	Validation	.8141 <sub>(.1301)</sub>	.8141 <sub>(.1301)</sub>	.8141 <sub>(.1301)</sub>	.8141 <sub>(.1301)</sub>	.8125 <sub>(.1329)</sub>	.8141 <sub>(.1301)</sub>	.8147 <sub>(.1299)</sub>	.8122 <sub>(.1358)</sub>	.8053 <sub>(.1374)</sub>	.6904 <sub>(.1614)</sub>	.6904 <sub>(.1614)</sub>
	Testing	.8146 <sub>(.1198)</sub>	.8146 <sub>(.1198)</sub>	.8146 <sub>(.1198)</sub>	.8146 <sub>(.1198)</sub>	.8130 <sub>(.1208)</sub>	.8146 <sub>(.1198)</sub>	.8154 <sub>(.1186)</sub>	.8119 <sub>(.1232)</sub>	.8050 <sub>(.1243)</sub>	.6870 <sub>(.1484)</sub>	.6870 <sub>(.1484)</sub>
f2 score	Validation	.7892 <sub>(.1381)</sub>	.7892 <sub>(.1371)</sub>	.7893 <sub>(.1371)</sub>	.7892 <sub>(.1381)</sub>	.7892 <sub>(.1372)</sub>	.7893 <sub>(.1381)</sub>	.7885 <sub>(.1381)</sub>	.7795 <sub>(.1489)</sub>	.7727 <sub>(.1515)</sub>	.7260 <sub>(.1475)</sub>	.7267 <sub>(.1485)</sub>
	Testing	.7926 <sub>(.1249)</sub>	.7926 <sub>(.1241)</sub>	.7926 <sub>(.1241)</sub>	.7925 <sub>(.1250)</sub>	.7925 <sub>(.1243)</sub>	.7926 <sub>(.1250)</sub>	.7928 <sub>(.1249)</sub>	.7822 <sub>(.1322)</sub>	.7738 <sub>(.1327)</sub>	.7284 <sub>(.1342)</sub>	.7293 <sub>(.1346)</sub>
Num. of Len-2 cycles	3	3	3	3	3	3	3	0	0	0	0	
Num. of Len-3 cycles	0	0	0	0	1	1	1	0	0	0	0	
Num. of Len-4 cycles	1	1	1	1	1	1	0	0	0	0	0	
Num. of Len-5 cycles	0	0	0	0	0	0	1	0	0	0	0	

Proposed variant of continuous DAG regularization.												
Hyperparameter $\lambda$	0	$10^{-6}$	$5 \times 10^{-6}$	$10^{-5}$	$5 \times 10^{-5}$	$10^{-4}$	<b><math>10^{-3}</math></b>	$10^{-2}$	$10^{-1}$	1	10	
AUROC	Validation	.9274 <sub>(.0656)</sub>	.9274 <sub>(.0656)</sub>	.9274 <sub>(.0656)</sub>	.9274 <sub>(.0656)</sub>	.9274 <sub>(.0656)</sub>	.9274 <sub>(.0656)</sub>	.9289 <sub>(.0635)</sub>	.9272 <sub>(.0652)</sub>	.9261 <sub>(.0674)</sub>	.9253 <sub>(.0685)</sub>	.9275 <sub>(.0638)</sub>
	Testing	.9297 <sub>(.0612)</sub>	.9297 <sub>(.0612)</sub>	.9297 <sub>(.0612)</sub>	.9297 <sub>(.0612)</sub>	.9297 <sub>(.0612)</sub>	.9297 <sub>(.0612)</sub>	.9307 <sub>(.0606)</sub>	.9296 <sub>(.0613)</sub>	.9286 <sub>(.0616)</sub>	.9274 <sub>(.0628)</sub>	.9294 <sub>(.0606)</sub>
AUPRC	Validation	.8496 <sub>(.1161)</sub>	.8496 <sub>(.1161)</sub>	.8496 <sub>(.1161)</sub>	.8496 <sub>(.1161)</sub>	.8496 <sub>(.1161)</sub>	.8496 <sub>(.1161)</sub>	.8504 <sub>(.1154)</sub>	.8498 <sub>(.1163)</sub>	.8498 <sub>(.1167)</sub>	.8494 <sub>(.1170)</sub>	.8496 <sub>(.1154)</sub>
	Testing	.8521 <sub>(.1062)</sub>	.8521 <sub>(.1063)</sub>	.8521 <sub>(.1063)</sub>	.8522 <sub>(.1062)</sub>	.8522 <sub>(.1062)</sub>	.8522 <sub>(.1062)</sub>	.8530 <sub>(.1063)</sub>	.8527 <sub>(.1067)</sub>	.8526 <sub>(.1066)</sub>	.8520 <sub>(.1072)</sub>	.8522 <sub>(.1064)</sub>
f1 score	Validation	.8141 <sub>(.1301)</sub>	.8141 <sub>(.1301)</sub>	.8141 <sub>(.1301)</sub>	.8141 <sub>(.1301)</sub>	.8141 <sub>(.1301)</sub>	.8141 <sub>(.1301)</sub>	.8138 <sub>(.1313)</sub>	.8140 <sub>(.1312)</sub>	.8135 <sub>(.1320)</sub>	.8130 <sub>(.1314)</sub>	.8139 <sub>(.1314)</sub>
	Testing	.8146 <sub>(.1198)</sub>	.8146 <sub>(.1198)</sub>	.8146 <sub>(.1198)</sub>	.8146 <sub>(.1198)</sub>	.8146 <sub>(.1198)</sub>	.8146 <sub>(.1198)</sub>	.8143 <sub>(.1200)</sub>	.8144 <sub>(.1201)</sub>	.8142 <sub>(.1203)</sub>	.8143 <sub>(.1202)</sub>	.8143 <sub>(.1202)</sub>
f2 score	Validation	.7892 <sub>(.1381)</sub>	.7892 <sub>(.1381)</sub>	.7892 <sub>(.1381)</sub>	.7892 <sub>(.1371)</sub>	.7892 <sub>(.1371)</sub>	.7893 <sub>(.1381)</sub>	.7889 <sub>(.1377)</sub>	.7889 <sub>(.1378)</sub>	.7894 <sub>(.1381)</sub>	.7893 <sub>(.1381)</sub>	.7893 <sub>(.1381)</sub>
	Testing	.7926 <sub>(.1249)</sub>	.7926 <sub>(.1249)</sub>	.7926 <sub>(.1249)</sub>	.7926 <sub>(.1241)</sub>	.7926 <sub>(.1241)</sub>	.7926 <sub>(.1249)</sub>	.7929 <sub>(.1249)</sub>	.7928 <sub>(.1251)</sub>	.7933 <sub>(.1252)</sub>	.7921 <sub>(.1249)</sub>	.7926 <sub>(.1249)</sub>
Num. of Len-2 cycles	3	3	3	3	3	3	0	0	0	0	0	
Num. of Len-3 cycles	0	0	0	0	0	0	0	0	0	0	0	
Num. of Len-4 cycles	1	1	1	1	1	1	0	0	0	0	0	
Num. of Len-5 cycles	0	0	0	0	0	0	0	0	0	0	0	

$\ell_1$ regularization.												
Hyperparameter $\lambda$	0	$10^{-6}$	$5 \times 10^{-6}$	$10^{-5}$	$5 \times 10^{-5}$	$10^{-4}$	$10^{-3}$	<b><math>10^{-2}</math></b>	$10^{-1}$	1	10	
AUROC	Validation	.9274 <sub>(.0656)</sub>	.9274 <sub>(.0656)</sub>	.9275 <sub>(.0656)</sub>	.9275 <sub>(.0655)</sub>	.9282 <sub>(.0634)</sub>	.9287 <sub>(.0624)</sub>	.9360 <sub>(.0599)</sub>	.9390 <sub>(.0579)</sub>	.9389 <sub>(.0578)</sub>	.9389 <sub>(.0578)</sub>	.9389 <sub>(.0578)</sub>
	Testing	.9297 <sub>(.0612)</sub>	.9297 <sub>(.0612)</sub>	.9298 <sub>(.0611)</sub>	.9298 <sub>(.0611)</sub>	.9306 <sub>(.0584)</sub>	.9312 <sub>(.0576)</sub>	.9381 <sub>(.0579)</sub>	.9397 <sub>(.0558)</sub>	.9397 <sub>(.0556)</sub>	.9397 <sub>(.0556)</sub>	.9397 <sub>(.0556)</sub>
AUPRC	Validation	.8496 <sub>(.1161)</sub>	.8496 <sub>(.1161)</sub>	.8496 <sub>(.1161)</sub>	.8496 <sub>(.1161)</sub>	.8497 <sub>(.1159)</sub>	.8497 <sub>(.1156)</sub>	.8513 <sub>(.1151)</sub>	.8524 <sub>(.1149)</sub>	.8524 <sub>(.1148)</sub>	.8524 <sub>(.1148)</sub>	.8524 <sub>(.1148)</sub>
	Testing	.8521 <sub>(.1062)</sub>	.8522 <sub>(.1062)</sub>	.8522 <sub>(.1062)</sub>	.8522 <sub>(.1062)</sub>	.8524 <sub>(.1059)</sub>	.8525 <sub>(.1067)</sub>	.8534 <sub>(.1069)</sub>	.8533 <sub>(.1076)</sub>	.8533 <sub>(.1074)</sub>	.8533 <sub>(.1074)</sub>	.8533 <sub>(.1074)</sub>
f1 score	Validation	.8141 <sub>(.1301)</sub>	.8141 <sub>(.1301)</sub>	.8141 <sub>(.1301)</sub>	.8141 <sub>(.1301)</sub>	.8129 <sub>(.1328)</sub>	.8133 <sub>(.1322)</sub>	.8135 <sub>(.1307)</sub>	.8134 <sub>(.1321)</sub>	.8134 <sub>(.1321)</sub>	.8134 <sub>(.1321)</sub>	.8134 <sub>(.1321)</sub>
	Testing	.8146 <sub>(.1198)</sub>	.8146 <sub>(.1198)</sub>	.8146 <sub>(.1198)</sub>	.8146 <sub>(.1198)</sub>	.8140 <sub>(.1207)</sub>	.8142 <sub>(.1201)</sub>	.8143 <sub>(.1203)</sub>	.8139 <sub>(.1207)</sub>	.8139 <sub>(.1207)</sub>	.8139 <sub>(.1207)</sub>	.8139 <sub>(.1207)</sub>
f2 score	Validation	.7892 <sub>(.1381)</sub>	.7892 <sub>(.1381)</sub>	.7893 <sub>(.1381)</sub>	.7893 <sub>(.1371)</sub>	.7893 <sub>(.1374)</sub>	.7892 <sub>(.1374)</sub>	.7881 <sub>(.1336)</sub>	.7893 <sub>(.1382)</sub>	.7893 <sub>(.1382)</sub>	.7893 <sub>(.1382)</sub>	.7893 <sub>(.1382)</sub>
	Testing	.7926 <sub>(.1249)</sub>	.7926 <sub>(.1249)</sub>	.7926 <sub>(.1249)</sub>	.7927 <sub>(.1240)</sub>	.7926 <sub>(.1246)</sub>	.7932 <sub>(.1249)</sub>	.7923 <sub>(.1222)</sub>	.7933 <sub>(.1256)</sub>	.7933 <sub>(.1256)</sub>	.7933 <sub>(.1256)</sub>	.7933 <sub>(.1256)</sub>
Num. of Len-2 cycles	3	3	2	2	2	3	0	0	0	0	0	
Num. of Len-3 cycles	0	0	0	0	0	0	0	0	0	0	0	
Num. of Len-4 cycles	1	1	1	1	1	3	0	0	0	0	0	
Num. of Len-5 cycles	0	0	0	0	0	0	0	0	0	0	0	

## 6.6 Result interpretation

The graphs in Figure 1 help to elucidate which relationships are most important in the graph, which is an essential aspect of interpretability. For example, the triggering effect from Diminished Cardiac Output (vital signs) to sepsis events remains to be significant after the uncertainty quantification and cycle elimination; in fact, nearly all triggering effects of sepsis events remain to be significant. Most importantly, we can identify several strong triggering effects shared by both graphs, which are commonly recognized (though in other types of patients). For example, the exciting effect from Hyperglycemia to Electrolyte Imbalance is commonly seen in type 2 diabetes patients Khan et al. [2019], and the observation that Acidosis precedes Cholestasis is common for patients with pregnancy Sterrenburg et al. [2014]. Those identified triggering effects agree with the well-known physiologic relationships and affirm the usefulness of our proposed method coupled with bootstrap uncertainty quantification and cycle elimination regularization.

Lastly, as shown in Tables 5 and 6, it is important to recognize that our model can predict not only upcoming sepsis events but also all SAD events in the graph. Even though our prediction of sepsis events is not perfect, the ability to predict other SADs which are on the path to sepsis or identify different potential pathways to an adverse event is also very important for clinicians to respond to those potential adverse events accordingly.

## 7 Conclusion

In this work, we present a generalized linear model for causal DAG discovery from mutually exciting time series data, which can be re-parameterized as a stochastic structural causal model with the Gumbel-Max technique. Most importantly, our proposed data-adaptive linear DAG-inducing regularization helps formulate the model estimation as a convex optimization problem. Furthermore, we establish a non-asymptotic estimation error upper bound for the GLM, which is verified numerically; we also give a confidence interval by solving linear programs. Both our numerical simulation and real data example show the good performance of our proposed method, making its future adoption in conducting continuous surveillance under medical settings and other similar problems much more likely.

There are a few interesting topics that the current work does not cover: On one hand, the convexity inherent in our proposed data-adaptive linear causal discovery method opens up the possibility of establishing performance guarantees; On the other hand, it is known that true DAG is only identifiable up to a Markov equivalence class from purely observational data

Verma and Pearl [2022] and it is of great interest to extend the current work by additionally considering interventional data Hauser and Bühlmann [2012], Brouillard et al. [2020] both methodology-wise and theory-wise. We leave those topics for future discussion.

## **Acknowledgment**

The work of Song Wei and Yao Xie is partially supported by an NSF CAREER CCF-1650913, and NSF DMS-2134037, CMMI-2015787, CMMI-2112533, DMS-1938106, DMS-1830210, and an Emory Hospital grant.

## A Extended Literature Survey

In this section, in addition to the literature survey on structural learning and Granger causality in Section 1.2, we review related works in causal discovery, causality for time series and Granger causality for point process data. To help readers understand how those areas connect with each other, we draw a diagram in Figure 6.

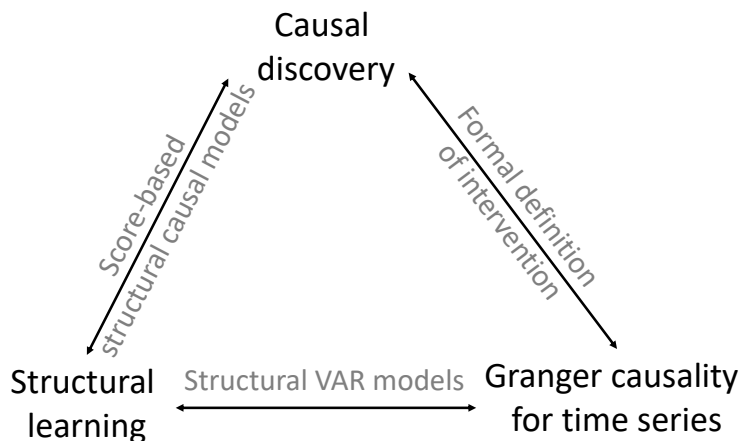


Figure 6: A diagram illustrating the connections among causal discovery, structural learning and Granger causality for time series.

*Causal inference.* Causal discovery from observational data mainly consists of constraint-based and score-based methods, aiming at finding causal relationships represented on DAGs Pearl [2009]. The state-of-the-art (conditional independence) constraint-based methods include PC, and Fast Causal Inference (FCI) Spirtes et al. [2000]. Both algorithms can output the underlying true DAG structure in the large sample limit. However, PC cannot deal with unobserved confounding, whereas FCI is capable of dealing with confounders. Since both algorithms rely on conditional independence tests to eliminate edges from the complete graph, they are not scalable when the number of nodes becomes large; existing methods to handle this include imposing sparse structure Kalisch and Bühlman [2007], leveraging the parallel computing technique Le et al. [2016], and score-based methods.

In score-based causal discovery methods, the first step is to define a score function measuring how well the model fits the observations, e.g., Bayesian Information Criterion (BIC), (log-)likelihood, and so on. For example, Greedy Equivalence Search Chickering [2002] starts with an empty graph and recursively adds/eliminates edges based on the BIC score. In particular, a line of research focuses on modeling the causal relationship using structural causal models (or structural equation models), and the joint probability distribution over a DAG



structure help define a log-likelihood score function. For example, Shimizu et al. [2006] studied a Linear, Non-Gaussian, Acyclic Model and proposed independent component analysis to infer the deterministic SCM with additive non-Gaussian noise; most importantly, Shimizu et al. [2006] discovered that linear-non-Gaussian assumption helps identify the full causal model. Another notable topic in this direction is the variational-inference-based approach for Bayesian causal discovery, where the difficulty comes from efficiently searching a combinatorially large DAG family to maximize the score. Examples include Cundy et al. [2021], who factorized the adjacency matrix into a permutation matrix and a strictly lower-triangular matrix to ensure DAG-ness, Lorch et al. [2021], Annadani et al. [2021], who leveraged a new algebraic characterization of DAG Zheng et al. [2018] in the prior distribution. In addition to the aforementioned causal discovery from observational data, there are also works focusing on recovering the causal graph from interventional data, where the log-likelihood score function is the joint interventional density. Notable contributions include Brouillard et al. [2020], who proposed a continuous optimization-based approach by leveraging the aforementioned continuous and differentiable DAG characterization Zheng et al. [2018]. For a systematic survey of recent developments on causal inference, we refer readers to Glymour et al. [2019].

*Causality for time series data.* When we consider observations exhibiting serial correlation, i.e., time series, Granger causality Granger [1969, 1980, 1988], which assesses whether the past of one time series is predictive of another, is a popular notion of causality due to its broad application, ranging from economics Chiou-Wei et al. [2008] and finance Hong et al. [2009], meteorology Mosedale et al. [2006], neuroscience Seth et al. [2015], health-care Wei et al. [2022] and so on. In the seminal work, Eichler and Didelez [2010] went beyond Granger causality by formally defining intervention and studying the causality in terms of the effect of the intervention on the VAR model. In addition to using the VAR model as the SCM, Peters et al. [2022] proposed an ordinary differential equation modification of SCM; Peters et al. [2022] also formally defined interventions and went beyond Granger causality to study the causality as the notion of interventional effect. However, they assumed known graph structure and did not answer the causal graph discovery question as SVAR models did. Thus, one may still need the aforementioned SVAR models to uncover the causal graph structure from observational time series data. Another line of research studied direction information, a generalized notion of Granger causality, as the notion of causality for time series data Quinn et al. [2011a,b, 2015]. Moreover, Quinn et al. [2011b] pointed out that both Granger causal graph and direction information graph is equivalent to minimal generative model graphs and, therefore, can be used for causal inference in the same manner as Bayesian networks are used

for correlative statistical inference. One limitation of the Granger causality framework comes from the no unobserved confounding assumption; existing efforts to tackle this issue include an FCI algorithm for time series to handle confounders Entner and Hoyer [2010].

*Granger causality for point process.* Recently, Kim et al. [2011] initiated the study of Granger causality for multivariate Hawkes Processes Hawkes [1971a,b], Hawkes and Oakes [1974], i.e., Hawkes network. Notable contributions include alternating direction method of multipliers coupled with low-rank structure in mutual excitation matrix Zhou et al. [2013], Fourier-transform based time series approach Etesami et al. [2016], expectation–maximization (EM) algorithm with various constraints Xu et al. [2016], Chen et al. [2022], Ide et al. [2021], Neural Network based approach Zhang et al. [2020], a regularized scalable gradient-based algorithm Wei et al. [2022], and so on. Our model is different from the aforementioned method in the following aspects: (i) Theoretically speaking, the guarantee is largely missing for Neural Network and EM-based methods — EM only maximizes a lower bound on log-likelihood and could converge to a local solution, let alone the Neural Network method. Moreover, EM is NOT scalable due to its quadratic complexity in the number of events. (ii) Practically speaking, our model handles multiple short time series sequences (most patients have short ICU stays, and the measurements are recorded hourly), whereas the aforementioned methods dealing with one long point process sequence cannot be easily reformulated to handle our target dataset. Nevertheless, we numerically compare with our previously proposed scalable gradient-based approach Wei et al. [2022] that shares a similar problem formulation with our method. Both our numerical simulation and real data example show our method has a better performance over the MHP method Wei et al. [2022], potentially due to the lack of granularity of time series data (compared with point process data).

## B Linear Program-based Confidence Interval

As pointed out in section II.E Juditsky et al. [2020], for general non-linear link function  $g$ , it would be hard to separate  $\theta_i$  from  $\sum_{t=1}^T w_{t-\tau:t-1} g(w_{t-\tau:t-1}^T \theta_i) / T$ . First, we derive a CI for linear link function case via a more precise data-driven bound for  $F_T^{(i)}(\theta_i) \in \mathbb{R}^d$  as Juditsky et al. [2020] did in Lemma 2 (see its proof in Appendix B):

**Proposition 3** (Confidence interval for linear transform of  $\theta_i$  for linear link function case). Under Assumptions 1 and 2, for  $i \in [d_1]$ , and every  $s > 1$ , the following holds with probability

at least  $1 - 2d\{s[\log((s-1)T) + 2] + 2\}e^{1-s}$ :

$$\theta_\ell[W_T, s; i] \leq a^\top \theta_i \leq \theta_u[W_T, s; i], \quad \forall a \in \mathbb{R}^d,$$

where  $\theta_\ell[W_T, s; i]$  and  $\theta_u[W_T, s; i]$  are defined in (24), (25).

This CI is obtained by solving LPs (24) and (25). For general non-linear link function  $g$ , since it is typically constrained in a compact subset to satisfy Assumption 1, we can obtain linear bounds on the non-linear link function and then repeat the above techniques to obtain similar CI.

*Proof.* We first define some notations:

$$\theta_\ell[W_T, s; i] = \min \left\{ \begin{array}{l} a^\top \theta_i : \theta_i \in \Theta, \\ \psi_\ell(a[W_T; i], T; s) \leq \frac{(\mathbb{W}_{1:T} \theta_i)_k}{M_w} \leq \psi_u(a[W_T; i], T; s), k \in [d_1]. \end{array} \right\} \quad (24)$$

$$\theta_u[W_T, s; i] = \max \left\{ \begin{array}{l} a^\top \theta_i : \theta_i \in \Theta, \\ \psi_\ell(a[W_T; i], T; s) \leq \frac{(\mathbb{W}_{1:T} \theta_i)_k}{M_w} \leq \psi_u(a[W_T; i], T; s), k \in [d_1]. \end{array} \right\} \quad (25)$$

Here,

$$\psi_\ell(\nu, d; y) = \begin{cases} (d+2y)^{-1} \left[ d\nu + \frac{2u}{3} - \sqrt{2d\nu y + \frac{y^2}{3} - \frac{2u}{d} \left( \frac{y}{3} - \nu d \right)^2} \right] & \text{if } \nu > \frac{y}{3d} \\ 0 & \text{otherwise} \end{cases}$$

$$\psi_u(\nu, d; y) = \begin{cases} (d+2y)^{-1} \left[ d\nu + \frac{4y}{3} + \sqrt{2d\nu y + \frac{5y^2}{3} - \frac{2y}{d} \left( \frac{y}{3} + \nu d \right)^2} \right] & \text{if } \nu < 1 - \frac{y}{3d} \\ 1 & \text{otherwise} \end{cases}$$

For  $i \in [d_1]$ , we will derive a more precise data-driven bound for  $F_T^{(i)}(\theta_i) \in \mathbb{R}^d$  as Juditsky et al. [2020] did in Lemma 2:

**Lemma 2.** Under Assumptions 1 and 2, for  $i \in [d_1]$ , and every  $s > 1$ , the following holds with probability at least  $1 - 2d\{s[\log((s-1)T) + 2] + 2\}e^{1-s}$ :

$$M_w \psi_\ell(a[W_T; i], T; s) \mathbf{1}_d - a[W_T; i] \leq F_T^{(i)}(\theta_i) \leq M_w \psi_u(a[W_T; i], T; s) \mathbf{1}_d - a[W_T; i],$$

where  $\mathbf{1}_d \in \mathbb{R}^d$  is the vector of ones, the inequality between vectors is element-wise, and

$$a[W_T; i] = \sum_{t=1}^T w_{t-\tau:t-1} y_t^{(i)} / T.$$

Then, it is easy to complete the proof, since by the above Lemma,  $\theta_i$  is a feasible solution to the linear programs (24) and (25) with probability at least  $1 - 2d\{s[\log((s-1)T) + 2] + 2\}e^{1-s}$ .  $\square$

*Proof of Lemma 2.* Similar to the proof of Lemma 2 Juditsky et al. [2020], we will make use of Lemma 4 therein to prove our Lemma 2 here.

We choose  $\gamma_t$  to be the  $k$ -th entry,  $k \in [d]$ , of  $w_{t-\tau:t-1}$  normalized by  $M_w$  such that it stays within  $[0, 1]$ , i.e.  $\gamma_i = (w_{t-\tau:t-1})_k / M_w$ . Then,  $\mu_t$  would be  $g(w_{t-\tau:t-1}^\top \theta_i)$  and  $\nu_t$  is the  $k$ -th entry of  $a[W_T; i]$  normalized by  $M_w$ , i.e.  $\nu_t = a[W_T; i]_k / M_w = \gamma_t y_t^{(i)}$ . By Lemma 4 Juditsky et al. [2020], we complete the proof.  $\square$

*Extension to general non-linear link function.* As for the general monotone non-linear link function, Lemma 4 still holds, but the vector field is no longer a linear transform of the coefficient vector. Nevertheless,  $\theta_i$  would still be a feasible solution to the following optimization problem with high probability:

$$\theta_\ell[W_T, s; i] = \min \left\{ \begin{array}{l} a^\top \theta_i : \theta_i \in \Theta, \\ \psi_\ell(a[W_T; i], T; s) \leq \frac{1}{TM_w} \sum_{t=1}^T (w_{t-\tau:t-1})_k g(w_{t-\tau:t-1}^\top \theta_i) \\ \leq \psi_u(a[W_T; i], T; s), k \in [d_1]. \end{array} \right\} \quad (26)$$

$$\theta_u[W_T, s; i] = \max \left\{ \begin{array}{l} a^\top \theta_i : \theta_i \in \Theta, \\ \psi_\ell(a[W_T; i], T; s) \leq \frac{1}{TM_w} \sum_{t=1}^T (w_{t-\tau:t-1})_k g(w_{t-\tau:t-1}^\top \theta_i) \\ \leq \psi_u(a[W_T; i], T; s), k \in [d_1]. \end{array} \right\} \quad (27)$$

However, even by assuming  $g$  to be convex or concave, we cannot say the above optimization is convex. So direct generalization may be problematic. Nevertheless, we could use linear bounds on the nonlinear link function such that we can still get a LP. Again, we take logistic regression as an example, where the link function is sigmoid function  $g(t) = \frac{1}{1+e^{-t}}$ : Let the upper and lower linear bound be  $f_1(x) = a_1x + b_1$  and  $f_2(x) = a_2x + b_2$ , respectively. we

have  $-a_1M + b_1 = 1/(1 + 1 + e^M)$  and  $-a_1(\log(1 + \sqrt{1 - 4a_1}) - \log(1 - \sqrt{1 - 4a_1})) + b_1 = (1 + \sqrt{1 - 4a_1})/2$ . Although we cannot give analytic solution, we can numerically solve this equation and obtain  $a_1, b_1$  and  $a_2, b_2$ .

## C Additional Details for Numerical Simulation

### C.1 Additional model training details

We give detailed configurations of the training procedure. For the PGD approach to solve for our proposed estimator, we use  $5 \times 10^{-3}$  as the initial learning rate and decrease it by half every 2000 iterations (in total, there are 6000 iterations). For simplicity, we assume we know that there does not exist inhibiting effect and perform PGD on the primal problem to solve for our proposed estimator, i.e., when learning for  $i$ -th node,  $i = [d_1]$ , we adopt feasible region  $\mathbb{R}_+^d$  and project negative entries back to zeros at each iteration in PGD; see detailed discussions in Sections 2.2, 2.4 and 3.3. Since there is no hyperparameter for the Mosek method, we do not give further instructions and refer readers to the documentation ApS [2019] on how to fit the model.

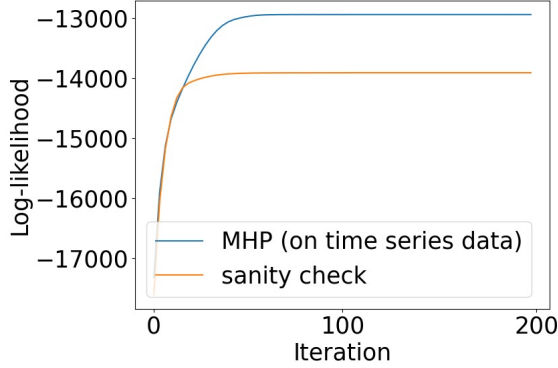
For the MHP benchmark method, we only adopt the first phase (which is PGD) proposed in Wei et al. [2022] to learn the parameters. We use  $2 \times 10^{-2}$  as the initial learning rate and decrease it by half every 100 iterations (in total, there are 200 iterations). We assume the decay parameter (i.e., the exponent in the exponential decay kernel) is known. In Figure 7 we plot the log-likelihood trajectories to verify the convergence.

For the NN-based method, we choose  $10^{-3}$  as the initial learning rate in total 2000 iterations. The hyperparameters are selected using grid search  $\mu_1 \in \{0.001, 0.01, 1\}$ ,  $\mu_2 \in \{0.001, 0.01, 1, 2\}$ ,  $\mu_3 \in \{0.001, 0.01, 1, 2\}$  and  $F = 60$ .

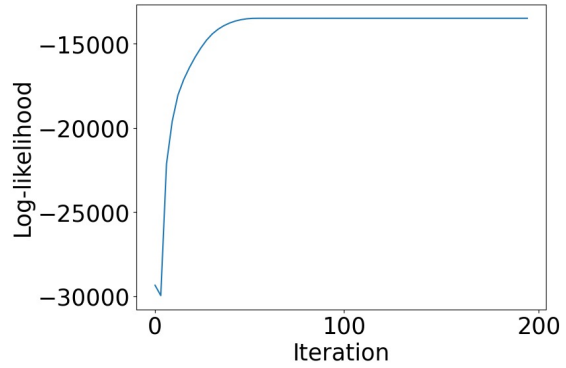
### C.2 Effectiveness of VI-based estimator: a sanity check

We consider time series data on time horizon  $T = 2000$  generated following our proposed linear model (3). The background intensity and the self- and mutual-exciting magnitude are visualized as ground truth in Figure 8. This setting serves as a sanity check, aiming to further demonstrate our proposed method works well under the correct model specification.

We visualize the recovered graphs in Figure 8 and report quantitative metrics in Table 8, where we can find  $(\text{VI}[F_T^{(i)}, \Theta])$  achieves the best result among all benchmark methods.



(a) Setting: point process data observed on discrete time grids.



(b) Setting: time series data.

Figure 7: Simulation: evidence of convergence for MHP benchmark methods. The left panel corresponds to Figure 2 and Table 2 and the right panel corresponds to Figure 8 and Table 8

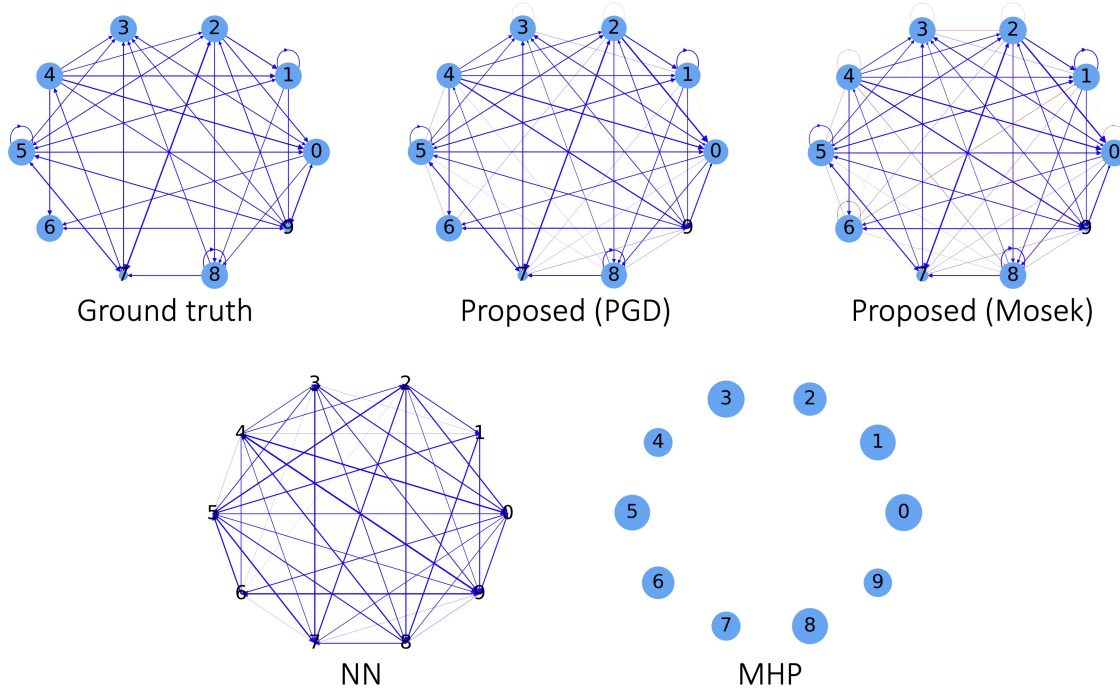


Figure 8: Simulated example: a sanity check to demonstrate of the effectiveness of  $VI[F_T^{(i)}, \Theta]$ . We visualize the recovered graph structures using our proposed VI-based estimator with linear link function as well as benchmark methods. We can observe that  $VI[F_T^{(i)}, \Theta]$  achieves the best recovery under the correct model specification; in contrast, NN cannot capture self-excitation, dad and MHP completely misses the interactions.

Table 8: Simulated example: quantitative metrics of the example in Figure 8. We can observe  $\text{VI}[F_T^{(i)}, \Theta]$  achieves the best results under the correct model specification.

Method	Proposed (PGD)	Proposed (Mosek)	NN	MHP
$\nu$ err.	<i>.054</i>	<b>.033</b>	—	.514
$A$ err.	<b>.106</b>	<i>.112</i>	.366	.594

### C.3 Effectiveness of PGD

As mentioned in Section 2.4, PGD can solve for  $\text{VI}[F_T^{(i)}, \Theta]$  with all monotone links. Despite the lack of theoretical guarantee, we use numerical evidence to show the good performance of PGD for all three link functions considered above: linear, sigmoid, and exponential links.

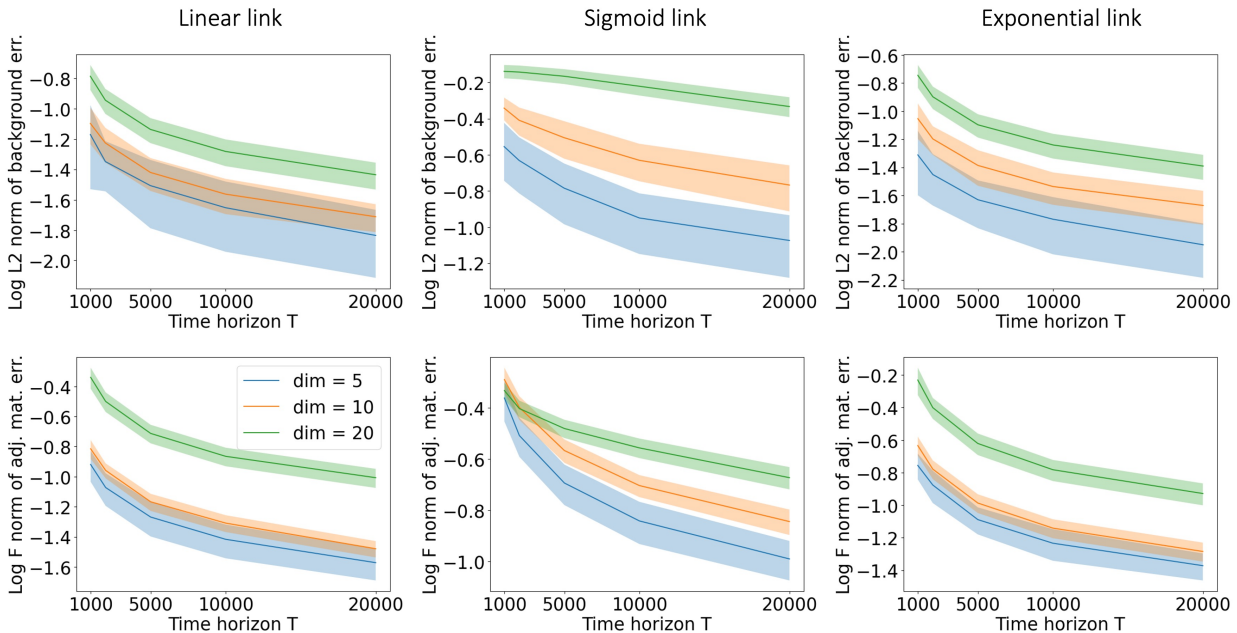


Figure 9: Simulation: mean (solid line) and standard deviation (shaded area) of estimation errors over 100 independent trials. We plot the  $\ell_2$  norm of the background intensity estimation error (the first row) and the matrix  $F$ -norm of the self- and mutual-exciting matrix estimation error (the second row). We can observe our proposed estimator obtained by PGD converges to the ground truth with increasing  $T$  for all types of links and graph size (dim) considered here.

Here, we use PGD to obtain our proposed estimator; the training procedure is the same as Experiment 1 and can be found in Appendix C.1. For each link function, we run 100 independent experiments for  $d_1 \in \{5, 10, 20\}$  over time horizons  $T \in \{1000, 2000, 5000, 10000, 20000\}$

with randomly generated ground truth parameters. We plot the mean and standard deviation of the  $\ell_2$  norm of the background intensity estimation error and the matrix  $F$ -norm of the self- and mutual-exciting matrix estimation error over those 100 independent trials in Figure 9. From this figure, we can observe that our proposed estimator obtained by PGD can converge to the ground truth with increasing  $T$ , which could serve as numerical evidence of the consistency of our proposed estimator. Moreover, the finite sample performances for the moderate-size graphs considered here are satisfying. Those evidence show the empirical success of PGD in obtaining our proposed estimator.

#### C.4 Effectiveness of our data-adaptive linear regularization

In this part of numerical simulation, the graph structure  $A$  is again randomly generated. To ensure the DAG-ness, we use  $A$  as initialization and apply vanilla gradient descent to minimize the DAG characterization  $h(A)$  and get  $\tilde{A}$  such that  $h(\tilde{A}) = 0$ . Finally, we set the diagonal elements  $\text{diag}(\tilde{A}) = \text{diag}(A)$  to maintain those self-exciting components.

Recall that we consider both linear and exponential link functions, where we can adopt the feasible region  $\tilde{\Theta} = \mathbb{R}_+^{d \times d_1}$ ; see the discussion in Section 3.3 on how to relax the constraints and adopt this feasible region in linear link case. Therefore, after the gradient descent update in each iteration, the projection back to  $\hat{\theta} \in \mathbb{R}_+^{d \times d_1}$  can be simply achieved by replacing all negative entries in  $\hat{\theta}$  with zeros. Further details such as the choice of learning rate  $\eta$  and total iteration number can be found in Appendix C.1 above.

The regularization strength hyperparameter  $\lambda$  is selected from  $\{1 \times 10^{-5}, 2 \times 10^{-5}, 3 \times 10^{-5}, 4 \times 10^{-5}, 5 \times 10^{-5}, 6 \times 10^{-5}, 7 \times 10^{-5}, 8 \times 10^{-5}, 9 \times 10^{-5}, 1 \times 10^{-4}, 2 \times 10^{-4}, 3 \times 10^{-4}, 4 \times 10^{-4}, 5 \times 10^{-4}, 6 \times 10^{-4}, 7 \times 10^{-4}, 8 \times 10^{-4}, 9 \times 10^{-4}, 1 \times 10^{-4}, 2 \times 10^{-4}, 3 \times 10^{-4}, 4 \times 10^{-4}, 5 \times 10^{-4}, 6 \times 10^{-4}, 7 \times 10^{-4}, 8 \times 10^{-4}, 9 \times 10^{-4}, 1 \times 10^{-2}, 2 \times 10^{-2}, 3 \times 10^{-2}, 4 \times 10^{-2}, 5 \times 10^{-2}, 6 \times 10^{-2}, 7 \times 10^{-2}, 8 \times 10^{-2}, 9 \times 10^{-2}, 1 \times 10^{-1}\}$ . We choose the one with the smallest  $A$  err. for each type of regularization.

In the  $d_1 = 10$  illustrative example, we plot the trajectories of all four metrics with varying hyperparameters in Figure 10. We can observe from this figure that (i) this hyperparameter selection method does give the best structure estimation, i.e., the smallest SHD, for our proposed data-adaptive linear approach; (ii) our proposed data-adaptive linear approach gives the most accurate structure estimation for a wide range of hyperparameters if we consider same regularization strength.

Lastly, we report all four metrics in our experiments with 100 trials in Table 9 for completeness.



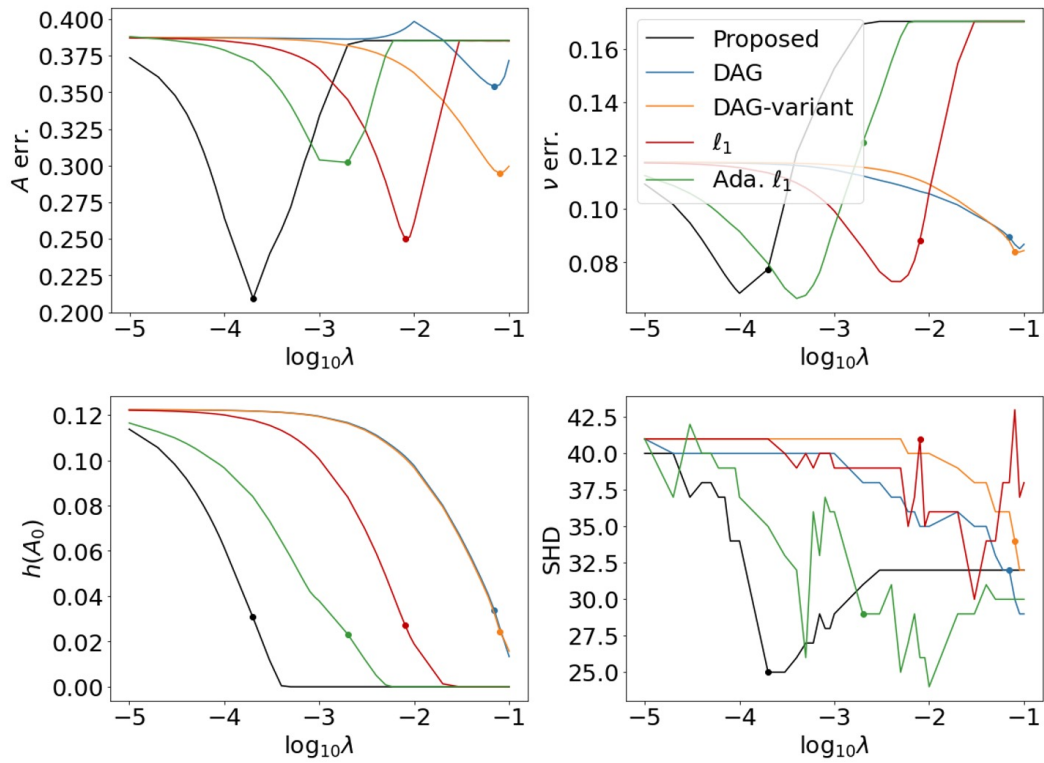


Figure 10: Simulation: the performance metrics with different hyperparameter  $\lambda$  for the illustrating example in Figure 3. In our numerical simulation,  $\lambda$  is selected to minimize  $A$  err., which is marked with a dot on all for panels for each type of regularization.

Table 9: Simulation: raw values of all metrics in Figure 4. We report the mean (and standard deviation) of all performance metrics over 100 trials for different types of regularization. We report the  $\ell_2$  norm of the background intensity estimation error ( $\nu$  err.), the matrix  $F$ -norm of the self- and mutual-exciting matrix estimation error ( $A$  err.), the DAG-ness measured by  $h(A_0)$  and the Structural Hamming Distance (SHD). We can observe that our proposed method does the best in terms of structure recovery whereas achieving almost the same performance with the best achievable weight recovery (by  $\ell_1$  regularization-based approach).

Linear link function case.  
Dimension  $d_1 = 10$ , Time Horizon  $T = 500$ .

Regularization	None	Proposed	DAG	DAG-Variant	$\ell_1$	Ada. $\ell_1$
$A$ err.	0.2510 <sub>(0.0502)</sub>	0.2015 <sub>(0.0374)</sub>	0.2372 <sub>(0.0498)</sub>	0.2253 <sub>(0.0518)</sub>	0.1968 <sub>(0.0335)</sub>	0.2063 <sub>(0.0403)</sub>
$\nu$ err.	0.1017 <sub>(0.0300)</sub>	0.0758 <sub>(0.0208)</sub>	0.0898 <sub>(0.0286)</sub>	0.0808 <sub>(0.0264)</sub>	0.0750 <sub>(0.0188)</sub>	0.0774 <sub>(0.0211)</sub>
$h(A_0)$	0.0586 <sub>(0.0190)</sub>	0.0183 <sub>(0.0133)</sub>	0.0336 <sub>(0.0253)</sub>	0.0051 <sub>(0.0111)</sub>	0.0190 <sub>(0.0129)</sub>	0.0142 <sub>(0.0138)</sub>
SHD	36.45 <sub>(5.32)</sub>	25.17 <sub>(5.28)</sub>	30.52 <sub>(7.99)</sub>	22.6 <sub>(6.39)</sub>	33.41 <sub>(5.02)</sub>	27.29 <sub>(5.17)</sub>

Dimension  $d_1 = 20$ , Time Horizon  $T = 1000$ .

Regularization	None	Proposed	DAG	DAG-Variant	$\ell_1$	Ada. $\ell_1$
$A$ err.	0.4403 <sub>(0.0669)</sub>	0.1442 <sub>(0.0408)</sub>	0.3879 <sub>(0.0704)</sub>	0.3955 <sub>(0.0694)</sub>	0.1293 <sub>(0.0376)</sub>	0.1323 <sub>(0.0402)</sub>
$\nu$ err.	0.1609 <sub>(0.0365)</sub>	0.0656 <sub>(0.0180)</sub>	0.1233 <sub>(0.0290)</sub>	0.1316 <sub>(0.0303)</sub>	0.0631 <sub>(0.0168)</sub>	0.0567 <sub>(0.0134)</sub>
$h(A_0)$	0.0425 <sub>(0.0106)</sub>	0.0011 <sub>(0.0021)</sub>	0.0006 <sub>(0.0002)</sub>	0.0006 <sub>(0.0002)</sub>	0.0013 <sub>(0.0024)</sub>	0.0002 <sub>(0.0006)</sub>
SHD	187.78 <sub>(11.80)</sub>	41.88 <sub>(19.24)</sub>	119.49 <sub>(8.96)</sub>	127.85 <sub>(9.73)</sub>	124.03 <sub>(33.37)</sub>	74.58 <sub>(24.35)</sub>

Exponential link function case.  
Dimension  $d_1 = 10$ , Time Horizon  $T = 500$ .

Regularization	None	Proposed	DAG	DAG-Variant	$\ell_1$	Ada. $\ell_1$
$A$ err.	0.3520 <sub>(0.1038)</sub>	0.2550 <sub>(0.0395)</sub>	0.3213 <sub>(0.0937)</sub>	0.3136 <sub>(0.1015)</sub>	0.2467 <sub>(0.0345)</sub>	0.2681 <sub>(0.0443)</sub>
$\nu$ err.	0.1125 <sub>(0.0326)</sub>	0.0854 <sub>(0.0231)</sub>	0.0929 <sub>(0.0300)</sub>	0.0917 <sub>(0.0280)</sub>	0.0835 <sub>(0.0204)</sub>	0.0924 <sub>(0.0241)</sub>
$h(A_0)$	0.0793 <sub>(0.0318)</sub>	0.0151 <sub>(0.0169)</sub>	0.0247 <sub>(0.0299)</sub>	0.0073 <sub>(0.0161)</sub>	0.0164 <sub>(0.0160)</sub>	0.0115 <sub>(0.0151)</sub>
SHD	36.83 <sub>(4.66)</sub>	24.18 <sub>(5.13)</sub>	28.03 <sub>(7.00)</sub>	24.16 <sub>(5.56)</sub>	32.9 <sub>(5.13)</sub>	26.78 <sub>(5.49)</sub>

Dimension  $d_1 = 20$ , Time Horizon  $T = 1000$ .

Regularization	None	Proposed	DAG	DAG-Variant	$\ell_1$	Ada. $\ell_1$
$A$ err.	0.5359 <sub>(0.0743)</sub>	0.1552 <sub>(0.0439)</sub>	0.4740 <sub>(0.0806)</sub>	0.4832 <sub>(0.0803)</sub>	0.1380 <sub>(0.0365)</sub>	0.1505 <sub>(0.0394)</sub>
$\nu$ err.	0.1778 <sub>(0.0376)</sub>	0.0706 <sub>(0.0151)</sub>	0.1355 <sub>(0.0296)</sub>	0.1443 <sub>(0.0302)</sub>	0.0680 <sub>(0.0152)</sub>	0.0655 <sub>(0.0133)</sub>
$h(A_0)$	0.0583 <sub>(0.0148)</sub>	0.0005 <sub>(0.0011)</sub>	0.0007 <sub>(0.0004)</sub>	0.0007 <sub>(0.0004)</sub>	0.0008 <sub>(0.0010)</sub>	0.0001 <sub>(0.0004)</sub>
SHD	186.86 <sub>(11.60)</sub>	35.1 <sub>(15.61)</sub>	116.28 <sub>(8.46)</sub>	124.51 <sub>(8.93)</sub>	118.57 <sub>(38.58)</sub>	66.15 <sub>(26.05)</sub>

## D Additional Details for Real Data Example

### D.1 Model comparison

*Training details for different models.* For our proposed method with linear link function, we leverage the prior knowledge that no inhibiting effect exists among SADs by projecting all negative iterates back to zeros when performing PGD on the primal problem, which is similar to what we have done in our numerical simulation. As for the second case, where we adopt the linear link function without using such prior knowledge, we use the well-developed package `Mosek` to learn the model parameters. For our proposed method with the sigmoid function, we again do not use the aforementioned prior knowledge and apply vanilla GD on the primal problem to obtain our proposed estimators. Detailed configurations of the training process are the same as our numerical simulation and already given in Appendix C.1 above; thus, we do not repeat them here.

As for the benchmark XGBoost method, we use the well-developed package `xgboost` Chen and Guestrin [2016] to fit the model. To be precise, we tune the hyperparameter using grid search over  $n\_estimators \in \{10, 20, 50, 500\}$ ,  $max\_depth \in \{None, 5, 20\}$ ,  $learning\_rate \in \{.0005, .001, .01\}$ ,  $subsample \in \{.3, .5\}$ ,  $colsample\_bytree \in \{.3, .5\}$ ,  $colsample\_bylevel \in \{.3, .5\}$  and  $colsample\_bynode \in \{.3, .5\}$ . Although there are other hyperparameters that we do not consider here, the main drawback of XGBoost is its explainability. Therefore, even though it might perform well on the prediction tasks (which was already validated in the 2019 Physionet Challenge Reyna et al. [2020]), it can not provide the clinician on why an alarm is raised.

*Additional results.* We report the recovered Granger causal graphs in Figure 11.

*Interpretation.* Figure 11 illustrates the resulting Granger causal graphs of SAD nodes that follow closely with known and expected causal relationships in sepsis-related illness. For example, the finding that Diminished Cardiac Output promotes sepsis events or that Tissue Ischemia strongly promotes Coagulopathy is well-appreciated relationships. The primary outcome of interest for this work was sepsis; still, as demonstrated in Figure 11, the causal relationship between any node pair can be estimated, giving clinician users insight into the probability of observing subsequent SADs after sepsis.

Figure 11 demonstrates the usefulness of prior medical knowledge in helping output a more sparse and interpretable graph structure (top left panel) compared with the rest two models (top right and bottom panels). Moreover, our proposed model with the sigmoid link

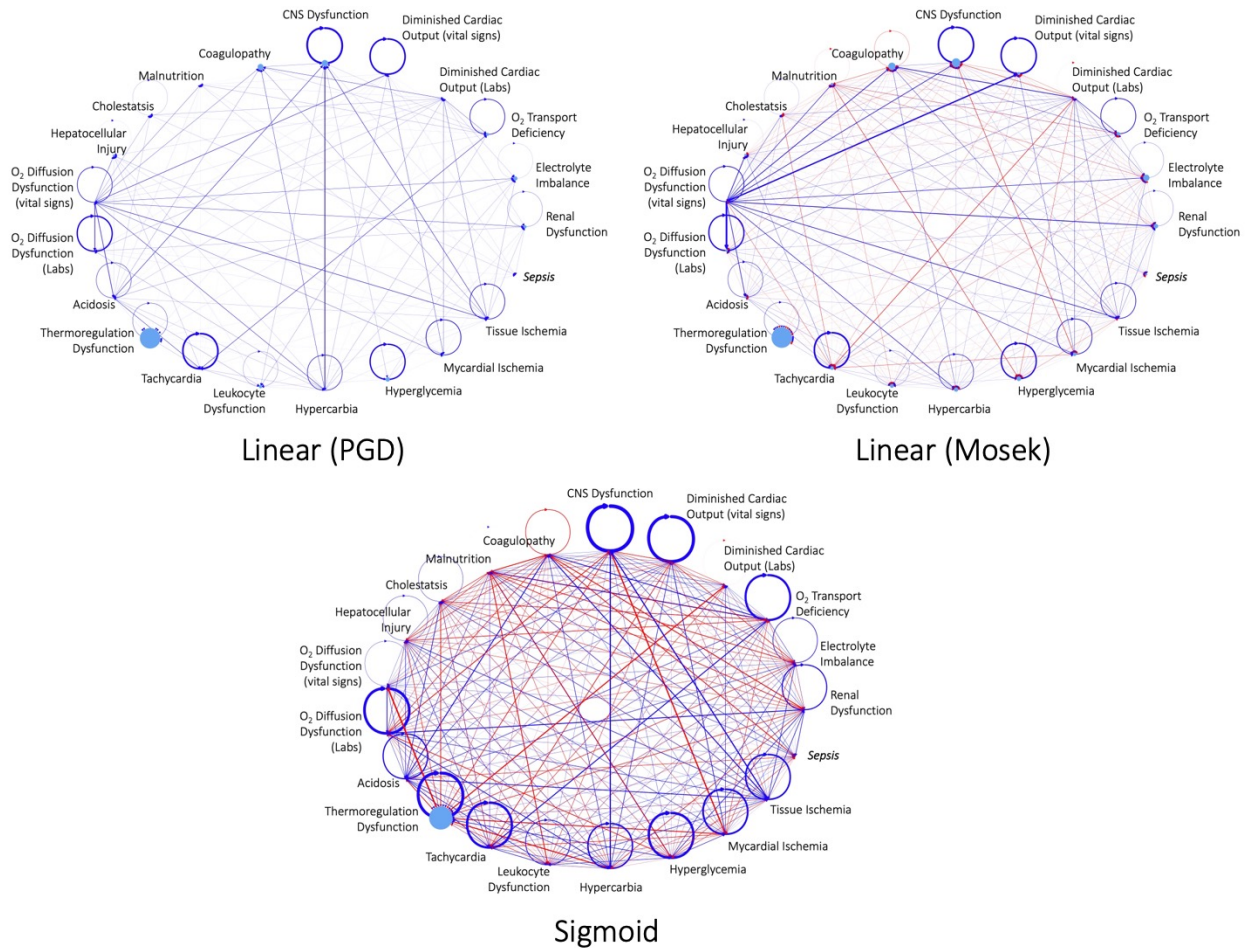


Figure 11: Granger causal graphs recovered by our proposed discrete-time Hawkes network using (i) linear link with prior knowledge that SADs can only promote each other (top left), (ii) linear link without prior knowledge (top right), and (iii) sigmoid link without prior knowledge (bottom). The size of the node is proportional to the background intensity, and the width of the directed edge is proportional to the exciting (blue) or inhibiting (red) effect magnitude. We can observe that prior medical knowledge that no inhibiting effect exists can help output a more sparse and interpretable graph structure; see the top left panel.

function seems to overestimate the interactions among SADs, making it difficult to extract useful information from the resulting Granger causal graph (bottom panel). Lastly, the graphs without using prior knowledge (top right and bottom panels) has identified relationships that suggest certain SADs actually have inhibitory effects. While there are possible explanations for these inhibitory effects, they are not commonly known or expected from a physiologic perspective. Overall, the graph that physicians’ prior knowledge demonstrates a more meaningful series of relationships consistent with known physiologic responses to sepsis.

## D.2 Uncertainty quantification

*Hyperparameter tuning.* The learning rate and total iteration number hyperparameters are selected by performing a grid search on  $\{.0002, .0004, \dots, .02\} \times \{1000, 2000, 5000, 10000, 20000\}$ . We choose the learning rate to be 0.0094 and the iteration number to be 2000, which maximizes the validation dataset AUROC.

Here, the performance metrics are not evaluated separately for each SAD; instead, we predict them all together and evaluate this “single-variable prediction” using the aforementioned metrics. The evaluation of f1 and f2 scores on the test dataset are based on cut-offs selected on the validation dataset (to maximize the validation f1 and f2 scores, respectively). Moreover, we calculate those metrics for every single patient and report the mean and standard deviation over all patients in the validation or test cohort. The results are in Tables 6 and 7.

*Bootstrap.* The bootstrap confidence intervals are obtained based on 1500 bootstrap samples. We sample 409 sepsis patients with equal probability with replacement from the original 409 sepsis patients in the year 2018 data; similarly, we draw 1369 non-sepsis patients uniformly with replacement from the original 1369 non-sepsis patients in the year 2018 data. For each bootstrap sample we obtained, we fit our proposed model. When we leverage the prior knowledge that no inhibiting effect exists, i.e., the PGD-based approach, we use the 5%-percentile and 100%-percentile of the bootstrap results as the 95% CI; otherwise, we use the 2.5%-percentile and 97.5%-percentile of the bootstrap results as the 95% CI. If the bootstrap CI contains zero, we then claim that such an edge does not exist and eliminate it in the graph. For those edges that exist, we use the median of the bootstrap results as the weight and plot the graph. A similar method applies to the background intensities.

*Additional results.* In addition to bootstrap for the PGD-based approach, we do the same thing for Mosek-based approach to further validate the usefulness of uncertainty quantification. The resulting graph is reported in Figure 12.

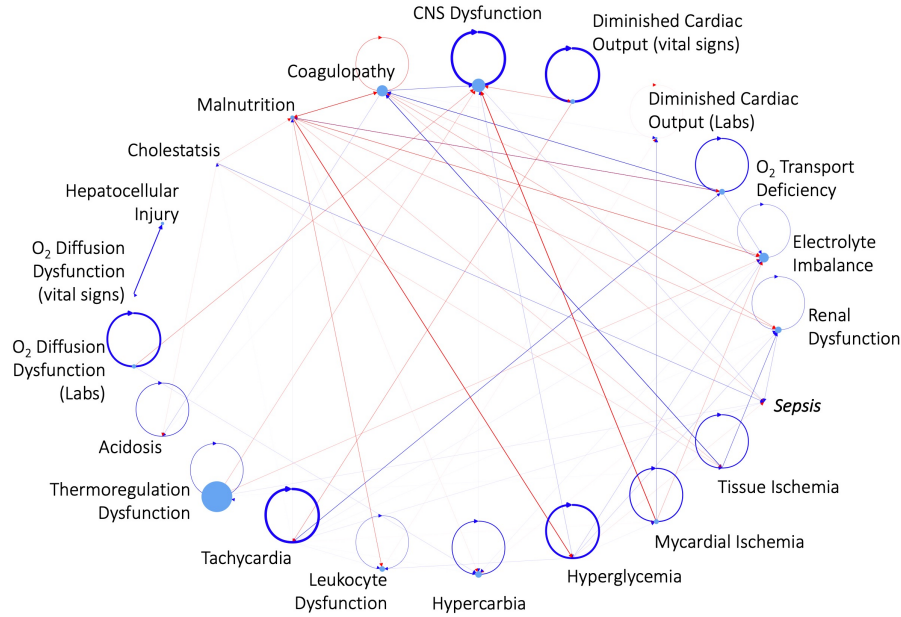


Figure 12: Granger causal graphs for SADs obtained via discrete-time Hawkes network using linear link coupled with bootstrap uncertainty quantification (confidence level is 95%). Here, we use package *Mosek* to learn the model parameters. We can observe that many inhibiting effects (which are hard to explain) disappear after bootstrap uncertainty quantification, suggesting the important of uncertainty quantification in practice.

From a physiologic perspective one would not normally expect a SAD to inhibit another SAD. While there could be unappreciated physiologic relationships or biases in the data that explain such an inhibitory relationship, these inhibitory relationships disappear (as seen in the second graph in Figure 12) with uncertainty quantification suggesting that they are not meaningful and should be eliminated. The elimination of inhibitory relationships further highlights the importance of uncertainty quantification.

## References

- ABIM. American board of internal medicine: Laboratory reference ranges. URL <https://www.abim.org/Media/bfijryql/laboratory-reference-ranges.pdf>.
- Yashas Annadani, Jonas Rothfuss, Alexandre Lacoste, Nino Scherrer, Anirudh Goyal, Yoshua Bengio, and Stefan Bauer. Variational causal networks: Approximate bayesian inference over causal structures. *arXiv preprint arXiv:2106.07635*, 2021.
- MOSEK ApS. *The MOSEK optimization toolbox for Python manual. Version 10.0.*, 2019. URL <https://docs.mosek.com/latest/pythonapi/index.html>.
- Sumanta Basu, Ali Shojaie, and George Michailidis. Network granger causality with inherent grouping structure. *The Journal of Machine Learning Research*, 16(1):417–453, 2015.
- Sumanta Basu, Xianqi Li, and George Michailidis. Low rank and structured modeling of high-dimensional vector autoregressions. *IEEE Transactions on Signal Processing*, 67(5):1207–1222, 2019.
- Andrew Bolstad, Barry D Van Veen, and Robert Nowak. Causal network inference via group sparse regularization. *IEEE transactions on signal processing*, 59(6):2628–2641, 2011.
- Philippe Brouillard, Sébastien Lachapelle, Alexandre Lacoste, Simon Lacoste-Julien, and Alexandre Drouin. Differentiable causal discovery from interventional data. *Advances in Neural Information Processing Systems*, 33:21865–21877, 2020.
- Tianqi Chen and Carlos Guestrin. XGBoost: A scalable tree boosting system. In *Proceedings of the 22nd ACM SIGKDD International Conference on Knowledge Discovery and Data Mining*, KDD ’16, pages 785–794, New York, NY, USA, 2016. ACM. ISBN 978-1-4503-4232-2. doi: 10.1145/2939672.2939785. URL <http://doi.acm.org/10.1145/2939672.2939785>.
- Wei Chen, Jibin Chen, Ruichu Cai, Yuequn Liu, and Zhifeng Hao. Learning granger causality for non-stationary hawkes processes. *Neurocomputing*, 468:22–32, 2022.
- David Maxwell Chickering. Optimal structure identification with greedy search. *Journal of machine learning research*, 3(Nov):507–554, 2002.
- Max Chickering, David Heckerman, and Chris Meek. Large-sample learning of bayesian networks is np-hard. *Journal of Machine Learning Research*, 5:1287–1330, 2004.

- Song Zan Chiou-Wei, Ching-Fu Chen, and Zhen Zhu. Economic growth and energy consumption revisited—evidence from linear and nonlinear granger causality. *Energy Economics*, 30(6):3063–3076, 2008.
- Chris Cundy, Aditya Grover, and Stefano Ermon. Bcd nets: Scalable variational approaches for bayesian causal discovery. *Advances in Neural Information Processing Systems*, 34: 7095–7110, 2021.
- John Anda Du, Nadi Sadr, and Philip de Chazal. Automated prediction of sepsis onset using gradient boosted decision trees. In *2019 Computing in Cardiology (CinC)*, pages Page–1. IEEE, 2019.
- Bradley Efron. *Exponential Families in Theory and Practice*. Cambridge University Press, 2022.
- Michael Eichler and Vanessa Didelez. On granger causality and the effect of interventions in time series. *Lifetime data analysis*, 16(1):3–32, 2010.
- Doris Entner and Patrik O Hoyer. On causal discovery from time series data using fci. *Probabilistic graphical models*, pages 121–128, 2010.
- Jalal Etesami, Negar Kiyavash, Kun Zhang, and Kushagra Singhal. Learning network of multivariate hawkes processes: a time series approach. In *Proceedings of the Thirty-Second Conference on Uncertainty in Artificial Intelligence*, pages 162–171, 2016.
- Zhuangyan Fang, Shengyu Zhu, Jiji Zhang, Yue Liu, Zhitang Chen, and Yangbo He. Low rank directed acyclic graphs and causal structure learning. *arXiv preprint arXiv:2006.05691*, 2020.
- Lucas M Fleuren, Thomas LT Klausch, Charlotte L Zwager, Linda J Schoonmade, Tingjie Guo, Luca F Roggeveen, Eleonora L Swart, Armand RJ Girbes, Patrick Thorat, Ari Ercole, et al. Machine learning for the prediction of sepsis: a systematic review and meta-analysis of diagnostic test accuracy. *Intensive care medicine*, 46(3):383–400, 2020.
- Clark Glymour, Kun Zhang, and Peter Spirtes. Review of causal discovery methods based on graphical models. *Frontiers in genetics*, 10:524, 2019.
- Clive WJ Granger. Investigating causal relations by econometric models and cross-spectral methods. *Econometrica: journal of the Econometric Society*, pages 424–438, 1969.



- Clive WJ Granger. Testing for causality: a personal viewpoint. *Journal of Economic Dynamics and control*, 2:329–352, 1980.
- Clive WJ Granger. Some recent development in a concept of causality. *Journal of econometrics*, 39(1-2):199–211, 1988.
- Michael Grant and Stephen Boyd. CVX: Matlab software for disciplined convex programming, version 2.1, 2014.
- Alain Hauser and Peter Bühlmann. Characterization and greedy learning of interventional markov equivalence classes of directed acyclic graphs. *The Journal of Machine Learning Research*, 13(1):2409–2464, 2012.
- Alan G Hawkes. Point spectra of some mutually exciting point processes. *Journal of the Royal Statistical Society: Series B (Methodological)*, 33(3):438–443, 1971a.
- Alan G Hawkes. Spectra of some self-exciting and mutually exciting point processes. *Biometrika*, 58(1):83–90, 1971b.
- Alan G Hawkes and David Oakes. A cluster process representation of a self-exciting process. *Journal of Applied Probability*, 11(3):493–503, 1974.
- Yongmiao Hong, Yanhui Liu, and Shouyang Wang. Granger causality in risk and detection of extreme risk spillover between financial markets. *Journal of Econometrics*, 150(2):271–287, 2009.
- Aapo Hyvärinen, Kun Zhang, Shohei Shimizu, and Patrik O Hoyer. Estimation of a structural vector autoregression model using non-gaussianity. *Journal of Machine Learning Research*, 11(5), 2010.
- Tsuyoshi Ide, Georgios Kollias, Dzung Phan, and Naoki Abe. Cardinality-regularized hawkes-granger model. *Advances in Neural Information Processing Systems*, 34, 2021.
- Eric Jang, Shixiang Gu, and Ben Poole. Categorical reparametrization with gumble-softmax. In *International Conference on Learning Representations*, 2017.
- Anatoli Juditsky, Arkadi Nemirovski, Liyan Xie, and Yao Xie. Convex parameter recovery for interacting marked processes. *IEEE Journal on Selected Areas in Information Theory*, 2020.

- Anatoli B Juditsky and AS Nemirovski. Signal recovery by stochastic optimization. *Automation and Remote Control*, 80(10):1878–1893, 2019.
- Markus Kalisch and Peter Bühlman. Estimating high-dimensional directed acyclic graphs with the pc-algorithm. *Journal of Machine Learning Research*, 8(3), 2007.
- Nan Rosemary Ke, Olexa Bilaniuk, Anirudh Goyal, Stefan Bauer, Hugo Larochelle, Bernhard Schölkopf, Michael C Mozer, Chris Pal, and Yoshua Bengio. Learning neural causal models from unknown interventions. *arXiv preprint arXiv:1910.01075*, 2019.
- Rashid Naseem Khan, Farhana Saba, Syedhh Fatima Kausar, and Muhammad Hassan Siddiqui. Pattern of electrolyte imbalance in type 2 diabetes patients: Experience from a tertiary care hospital. *Pakistan Journal of Medical Sciences*, 35(3):797, 2019.
- Saurabh Khanna and Vincent YF Tan. Economy statistical recurrent units for inferring nonlinear granger causality. In *International Conference on Learning Representations*, 2019.
- Sanggyun Kim, David Putrino, Soumya Ghosh, and Emery N Brown. A granger causality measure for point process models of ensemble neural spiking activity. *PLoS computational biology*, 7(3):e1001110, 2011.
- Neville K Kitson, Anthony C Constantinou, Zhigao Guo, Yang Liu, and Kiattikun Chobtham. A survey of bayesian network structure learning. *arXiv preprint arXiv:2109.11415*, 2021.
- Sébastien Lachapelle, Philippe Brouillard, Tristan Deleu, and Simon Lacoste-Julien. Gradient-based neural dag learning. In *International Conference on Learning Representations*, 2019.
- Thuc Duy Le, Tao Hoang, Jiuyong Li, Lin Liu, Huawen Liu, and Shu Hu. A fast pc algorithm for high dimensional causal discovery with multi-core pcs. *IEEE/ACM transactions on computational biology and bioinformatics*, 16(5):1483–1495, 2016.
- Po-Ling Loh and Peter Bühlmann. High-dimensional learning of linear causal networks via inverse covariance estimation. *The Journal of Machine Learning Research*, 15(1):3065–3105, 2014.
- Guy Lorberbom, Daniel D Johnson, Chris J Maddison, Daniel Tarlow, and Tamir Hazan. Learning generalized gumbel-max causal mechanisms. *Advances in Neural Information Processing Systems*, 34:26792–26803, 2021.

- Lars Lorch, Jonas Rothfuss, Bernhard Schölkopf, and Andreas Krause. Dibs: Differentiable bayesian structure learning. *Advances in Neural Information Processing Systems*, 34, 2021.
- Helmut Lütkepohl. *New introduction to multiple time series analysis*. Springer Science & Business Media, 2005.
- C Maddison, A Mnih, and Y Teh. The concrete distribution: A continuous relaxation of discrete random variables. In *Proceedings of the international conference on learning Representations*, 2017.
- Hasan Manzour, Simge Küçükyavuz, Hao-Hsiang Wu, and Ali Shojaie. Integer programming for learning directed acyclic graphs from continuous data. *INFORMS Journal on Optimization*, 3(1):46–73, 2021.
- Timothy J Mosedale, David B Stephenson, Matthew Collins, and Terence C Mills. Granger causality of coupled climate processes: Ocean feedback on the north atlantic oscillation. *Journal of climate*, 19(7):1182–1194, 2006.
- Ignavier Ng, AmirEmad Ghassami, and Kun Zhang. On the role of sparsity and dag constraints for learning linear dags. *Advances in Neural Information Processing Systems*, 33:17943–17954, 2020.
- Kimia Noorbakhsh and Manuel Gomez Rodriguez. Counterfactual temporal point processes. *arXiv preprint arXiv:2111.07603*, 2021.
- Michael Oberst and David Sontag. Counterfactual off-policy evaluation with gumbel-max structural causal models. In *International Conference on Machine Learning*, pages 4881–4890. PMLR, 2019.
- Roxana Pamfil, Nisara Sriwattanaworachai, Shaan Desai, Philip Pilgerstorfer, Konstantinos Georgatzis, Paul Beaumont, and Bryon Aragam. Dynotears: Structure learning from time-series data. In *International Conference on Artificial Intelligence and Statistics*, pages 1595–1605. PMLR, 2020.
- Judea Pearl. *Causality*. Cambridge university press, 2009.
- Jonas Peters, Stefan Bauer, and Niklas Pfister. Causal models for dynamical systems. In *Probabilistic and Causal Inference: The Works of Judea Pearl*, pages 671–690. 2022.

- Christopher J Quinn, Todd P Coleman, Negar Kiyavash, and Nicholas G Hatsopoulos. Estimating the directed information to infer causal relationships in ensemble neural spike train recordings. *Journal of computational neuroscience*, 30(1):17–44, 2011a.
- Christopher J Quinn, Negar Kiyavash, and Todd P Coleman. Equivalence between minimal generative model graphs and directed information graphs. In *2011 IEEE International Symposium on Information Theory Proceedings*, pages 293–297. IEEE, 2011b.
- Christopher J Quinn, Negar Kiyavash, and Todd P Coleman. Directed information graphs. *IEEE Transactions on information theory*, 61(12):6887–6909, 2015.
- M. A. Reyna, C. S. Josef, R. Jeter, S. P. Shashikumar, M. B. Westover, S. Nemati, G. D. Clifford, and A. Sharma. Early Prediction of Sepsis From Clinical Data: The PhysioNet/Computing in Cardiology Challenge 2019. *Crit Care Med*, 48(2):210–217, 02 2020.
- Matthew A Reyna, Chris Josef, Salman Seyedi, Russell Jeter, Supreeth P Shashikumar, M Brandon Westover, Ashish Sharma, Shamim Nemati, and Gari D Clifford. Early prediction of sepsis from clinical data: the physionet/computing in cardiology challenge 2019. In *2019 Computing in Cardiology (CinC)*, pages Page–1. IEEE, 2019.
- Mauro Scanagatta, Antonio Salmerón, and Fabio Stella. A survey on bayesian network structure learning from data. *Progress in Artificial Intelligence*, 8(4):425–439, 2019.
- Bernhard Schölkopf, Francesco Locatello, Stefan Bauer, Nan Rosemary Ke, Nal Kalchbrenner, Anirudh Goyal, and Yoshua Bengio. Toward causal representation learning. *Proceedings of the IEEE*, 109(5):612–634, 2021.
- Anil K Seth, Adam B Barrett, and Lionel Barnett. Granger causality analysis in neuroscience and neuroimaging. *Journal of Neuroscience*, 35(8):3293–3297, 2015.
- Christopher W. Seymour, Foster Gesten, Hallie C. Prescott, Marcus E. Friedrich, Theodore J. Iwashyna, Gary S. Phillips, Stanley Lemeshow, Tiffany Osborn, Kathleen M. Terry, and Mitchell M. Levy. Time to Treatment and Mortality during Mandated Emergency Care for Sepsis. *N. Engl. J. Med.*, 376(23):2235–2244, 2017. ISSN 1533-4406. doi: 10.1056/NEJMoa1703058.
- Supreeth P. Shashikumar, Christopher S. Josef, Ashish Sharma, and Shamim Nemati. DeepAISE – An interpretable and recurrent neural survival model for early prediction of sepsis. *Artificial Intelligence in Medicine*, 113:102036, March 2021. ISSN 0933-3657.

doi: 10.1016/j.artmed.2021.102036. URL <https://www.sciencedirect.com/science/article/pii/S0933365721000294>.

Shohei Shimizu, Patrik O Hoyer, Aapo Hyvärinen, Antti Kerminen, and Michael Jordan. A linear non-gaussian acyclic model for causal discovery. *Journal of Machine Learning Research*, 7(10), 2006.

Ali Shojaie and Emily B Fox. Granger causality: A review and recent advances. *Annual Review of Statistics and Its Application*, 9:289–319, 2022.

Vikas Sindhwani, Ha Quang Minh, and Aurélie C Lozano. Scalable matrix-valued kernel learning for high-dimensional nonlinear multivariate regression and granger causality. In *Proceedings of the Twenty-Ninth Conference on Uncertainty in Artificial Intelligence*, pages 586–595, 2013.

Mervyn Singer, Clifford S Deutschman, Christopher Warren Seymour, Manu Shankar-Hari, Djillali Annane, Michael Bauer, Rinaldo Bellomo, Gordon R Bernard, Jean-Daniel Chiche, Craig M Coopersmith, et al. The third international consensus definitions for sepsis and septic shock (sepsis-3). *Jama*, 315(8):801–810, 2016.

Pater Spirtes, Clark Glymour, Richard Scheines, Stuart Kauffman, Valerio Aimale, and Frank Wimberly. Constructing bayesian network models of gene expression networks from microarray data. 2000.

Karin Sterrenburg, Willy Visser, LS Smit, and Jérôme Cornette. Acidosis: A potential explanation for adverse fetal outcome in intrahepatic cholestasis of pregnancy. a case report. *Obstetric Medicine*, 7(4):177–179, 2014.

Alex Tank, Ian Covert, Nicholas Foti, Ali Shojaie, and Emily Fox. Neural granger causality for nonlinear time series. *stat*, 1050:16, 2018.

Alex Tank, Emily B Fox, and Ali Shojaie. Identifiability and estimation of structural vector autoregressive models for subsampled and mixed-frequency time series. *Biometrika*, 106(2): 433–452, 2019.

Alexander Tong, Lazar Atanackovic, Jason Hartford, and Yoshua Bengio. Bayesian dynamic causal discovery. In *A causal view on dynamical systems, NeurIPS 2022 workshop*.

Thomas S Verma and Judea Pearl. Equivalence and synthesis of causal models. In *Probabilistic and Causal Inference: The Works of Judea Pearl*, pages 221–236. 2022.

- Matthew J Vowels, Necati Cihan Camgoz, and Richard Bowden. D’ya like dags? a survey on structure learning and causal discovery. *ACM Computing Surveys*, 55(4):1–36, 2022.
- Song Wei, Yao Xie, Christopher S Josef, and Rishikesan Kamaleswaran. Causal graph recovery for sepsis-associated derangements via interpretable hawkes networks. In *International Conference on Machine Learning, Workshop on Interpretable Machine Learning in Healthcare (IMLH)*, 2021a.
- Song Wei, Yao Xie, and Dobromir Rahnev. Inferring serial correlation with dynamic backgrounds. In *International Conference on Machine Learning*, pages 11047–11057. PMLR, 2021b.
- Song Wei, Yao Xie, Christopher S Josef, and Rishikesan Kamaleswaran. Granger causal chain discovery for sepsis-associated derangements via multivariate hawkes processes. *arXiv preprint arXiv:2209.04480*, 2022.
- WHO. Global report on the epidemiology and burden of sepsis: current evidence, identifying gaps and future directions. 2020.
- Jing Xiang and Seyoung Kim. A\* lasso for learning a sparse bayesian network structure for continuous variables. *Advances in neural information processing systems*, 26, 2013.
- Hongteng Xu, Mehrdad Farajtabar, and Hongyuan Zha. Learning granger causality for hawkes processes. In *International Conference on Machine Learning*, pages 1717–1726. PMLR, 2016.
- Meicheng Yang, Chengyu Liu, Xingyao Wang, Yuwen Li, Hongxiang Gao, Xing Liu, and Jianqing Li. An explainable artificial intelligence predictor for early detection of sepsis. *Critical Care Medicine*, 48(11):e1091–e1096, 2020.
- Yue Yu, Jie Chen, Tian Gao, and Mo Yu. Dag-gnn: Dag structure learning with graph neural networks. In *International Conference on Machine Learning*, pages 7154–7163. PMLR, 2019.
- Yiping Yuan, Xiaotong Shen, Wei Pan, and Zizhuo Wang. Constrained likelihood for reconstructing a directed acyclic gaussian graph. *Biometrika*, 106(1):109–125, 2019.
- Morteza Zabihi, Serkan Kiranyaz, and Moncef Gabbouj. Sepsis prediction in intensive care unit using ensemble of xgboost models. In *2019 Computing in Cardiology (CinC)*, pages Page–1. IEEE, 2019.

- Kun Zhang and Aapo Hyvärinen. Causality discovery with additive disturbances: An information-theoretical perspective. In *Joint European Conference on Machine Learning and Knowledge Discovery in Databases*, pages 570–585. Springer, 2009.
- Wei Zhang, Thomas Panum, Somesh Jha, Prasad Chalasani, and David Page. Cause: Learning granger causality from event sequences using attribution methods. In *International Conference on Machine Learning*, pages 11235–11245. PMLR, 2020.
- Xun Zheng, Bryon Aragam, Pradeep K Ravikumar, and Eric P Xing. Dags with no tears: Continuous optimization for structure learning. *Advances in Neural Information Processing Systems*, 31, 2018.
- Ke Zhou, Hongyuan Zha, and Le Song. Learning social infectivity in sparse low-rank networks using multi-dimensional hawkes processes. In *Artificial Intelligence and Statistics*, pages 641–649. PMLR, 2013.
- Hui Zou. The adaptive lasso and its oracle properties. *Journal of the American statistical association*, 101(476):1418–1429, 2006.